Autonomous Integrity Monitoring for Vehicular Navigation With Cellular Signals of Opportunity and an IMU

Mahdi Maaref and Zaher M. Kassas, *Senior Member, IEEE*

***Abstract*— A receiver autonomous integrity monitoring (RAIM) framework for ground vehicle navigation using ambient cellular signals of opportunity (SOPs) and an inertial measurement unit (IMU) is developed. The proposed framework accounts for two types of errors that compromise the integrity of the navigation solution: (i) multipath and (ii) unmodeled biases in the cellular pseudorange measurements due to line-of-sight (LOS) signal blockage and high signal attenuation. This paper, first, characterizes the multipath in a cellular-based navigation framework. Next, a fault detection and exclusion technique for a cellular-based navigation framework is developed. Simulation and experimental results with real long-term evolution (LTE) signals are presented evaluating the efficacy of the proposed RAIM-based fault detection and exclusion technique on a ground vehicle navigating in a deep urban environment in the absence of global navigation satellite system (GNSS) signals. The experimental results on a ground vehicle traversing 825 m in an urban environment show that the proposed RAIM-based measurement exclusion technique reduces the position root mean-squared error (RMSE) by 66%.**

***Index Terms*— Navigation, ground vehicle, receiver autonomous integrity monitoring, signals of opportunity.**

I. Introduction

VARIOUS sensing modalities have been developed to provide more accurate vehicular navigational information. These sensing modalities can be classified into two major categories: (i) local sensing modalities, which provide the location of the ground vehicle relative to its own coordinate system and (ii) global sensing modalities, which provide the absolute location of the ground vehicle within a global frame. In recent years, filter-based frameworks [1] as well as graph optimization-based frameworks [2], [3] have been developed to fuse local and global sensing modality sensor data. From a vehicular navigation perspective, the global sensing modality has been monopolized by global navigation satellite systems (GNSS). However, the GNSS navigation solution significantly degrades in deep urban canyons [4], [5]. In light of recent studies, signals of opportunity (SOPs) have been introduced as another fruitful class of global sensing modality [6]–[8] to overcome GNSS limitation. SOPs are radio frequency (RF) signals that are not intended for navigation but can be exploited for navigation purposes, especially in GNSS-challenged environments. SOPs include a wide range of signals such as AM/FM radio, digital television, cellular, and low Earth orbit (LEO) satellites signals [9]–[12]. Among these signals, cellular signals are particularly attractive due to their desirable characteristics, including (i) abundance in urban canyons, (ii) geometric diversity, (iii) high received power, and (iv) large bandwidth [13]. These characteristics make cellular signals desirable sources for navigation, either as a complement or alternative to GNSS signals [14]. Previous work has studied the accuracy and availability of these signals [15]. Recent research results have demonstrated meter-level accurate navigation with cellular SOPs on ground vehicles [14], [16], [17] and centimeter-level accurate navigation on aerial vehicles [18]–[20].

As vehicles approach autonomous driving with less human-in-the-loop, the need for monitoring the integrity of their navigation solution increases. According to the SAE J3016 standard, automation levels 4 and 5 require the vehicle to be capable of performing centimeter-level driving functions independently and self-sufficiently. This level of automation cannot be achieved without a precise measure of trustworthiness of the navigation solution, which is assessed by the integrity monitoring system. Integrity monitoring refers to one of the methods to detect anomalies and warn the user when the system should not be used [21]. A high-integrity navigation system must be able to reject incorrect measurements and provide an integrity metric of the confidence in the system performance at any time. Integrity monitoring for ground vehicles has been the subject of many recent studies, and different schemes that incorporate different sensing modalities have been proposed, such as multi-constellation (e.g., Galileo-GPS [22] and GLONASS-GPS [23]), INS-GPS [24], and lidar-GPS [25]. As the number of systems that rely on SOPs for navigation grows, developing integrity monitoring frameworks for SOP-GPS becomes essential. Similar to the integrity of the GNSS-based navigation solution, the most pressing concern in integrity monitoring of an SOP-based navigation solution is the user's ability to recognize when it is safe to use the system. Fig. 1 illustrates a cellular SOP-based integrity monitoring

Manuscript received January 16, 2020; revised June 8, 2020, October 25, 2020, and December 23, 2020; accepted January 15, 2021. Date of publication February 17, 2021; date of current version May 31, 2022. This work was supported in part by the National Science Foundation (NSF) under Grant 1929965 and in part by the Office of Naval Research (ONR) under Grant N00014-19-1-2613 and Grant N00014-19-1-2511. The Associate Editor for this article was G. Mao. *(Corresponding author: Zaher M. Kassas.)*

Mahdi Maaref is with the Department of Mechanical and Aerospace Engineering, UCI, Irvine, CA 92617 USA (e-mail: mmaaref@uci.edu).

Zaher M. Kassas is with the Department of Mechanical and Aerospace Engineering, UCI, Irvine, CA 92617 USA, and also with the EECS Department, UCI, Irvine, CA 92617 USA (e-mail: zkassas@ieee.org).

Digital Object Identifier 10.1109/TITS.2021.3055200

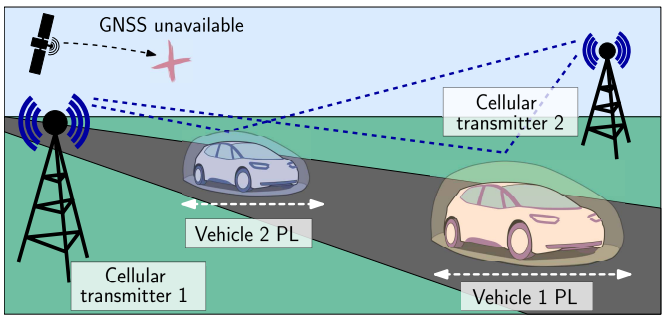

Fig. 1. A cellular SOP-based integrity monitoring framework in a GNSS-challenged environment. In the absence of GNSS signals, received cellular signals are used for navigation as well as calculating the integrity measures.

framework in a GNSS-challenged environment, where in the absence of the GNSS signals, the received cellular signals are used for (i) obtaining the navigation solution and (ii) calculating the integrity measures.

Integrity monitoring frameworks are divided into two categories: internal and external [26]. External methods (e.g., ground-based augmentation system (GBAS), satellite-based augmentation system (SBAS), etc.) leverage a network of ground monitoring stations to monitor the transmitted signals, while internal methods (e.g., receiver autonomous integrity monitoring (RAIM)) typically use the redundant information within the transmitted navigation signals. Among several methods developed to monitor system's integrity, RAIM inherently possess desirable characteristics, particularly for ground-based receivers in urban canyons, due to its design flexibility and adaptability to the urban environment [27], [28]. In contrast to external integrity monitoring methods, RAIM alleviates the need for costly, bulky, and computationally intensive infrastructure. RAIM detects GNSS pseudorange measurement faults by only exploiting the redundancy of GNSS signals to check the measurements' consistency. RAIM can also be coupled with the output of other navigation sensors to enhance the system's integrity [29].

Initial work on integrity monitoring for cellular long-term evolution (LTE) signals-based navigation was conducted in [15], [30], where the integrity of the LTE-based navigation solution was studied. This paper extends the previous work through the following contributions. First, the previous work assumed the presence of a stationary agent in the vehicle's environment, referred to as the base, which has knowledge of its own state at all time. The base's purpose was to estimate the dynamic stochastic clock errors of cellular transmitters and to share these estimates with the navigating vehicle. It was assumed that base is available in the same cellular environment of the navigating vehicle, and it has direct line-of-sight (LOS) to all of the cellular towers. This assumption could be impractical in some real-world environments. Therefore, developing a self-contained solution will be desirable. In contrast to the method presented in [15], this paper develops a self-contained navigation framework, which simultaneously localizes the receiver and estimates the receiver's and transmitters' clock errors. This estimation problem is referred to as radio simultaneous localization and mapping (SLAM) and is analogous to the SLAM problem in robotics. However, in contrast to the static feature map of the typical SLAM problem, the radio SLAM signal landscape map consists of dynamic stochastic states (namely, clock bias and drift). Second, a method to model multipath in cellular SOP-based RAIM frameworks is presented. Third, this paper analytically evaluates and models the test statistic as well as the horizontal protection level with cellular SOPs. Accordingly, a fault detection and exclusion technique is presented. The paper assumes the existence of a single fault bias induced into the measurements, due to LOS blockage. For complicated wireless environments with multiple faults, more sophisticated methods must be employed. Fourth, the accuracy and efficacy of the proposed framework under different fault conditions is analyzed through different simulations and an experimental tests. The experimental test uses real LTE signals and is conducted on a ground vehicle traversing 825 m in an urban environment. The experimental results show that the proposed RAIM-based measurement exclusion technique reduces the position root mean-squared error (RMSE) by 66%.

This paper considers the following practical scenario. A ground vehicle is equipped with an inertial measurement unit (IMU), a GNSS receiver, and a separate receiver capable of producing pseudoranges to ambient cellular transmitters. When the vehicle enters a GNSS-challenged environments (e.g., a deep urban canyon or an environment affected by a malicious jamming attack on the GNSS frequency band), GNSS signals are no longer usable or reliable. In the absence of GNSS measurements, the accumulated error of the IMU grows unboundedly. However, cellular SOPs can be used as an aiding source to bound the navigation errors [31], [32]. It is worth noting that the proposed approach shows how cellular pseudoranges can be used as an aiding source for an IMU in a global frame in the absence of GNSS signals. The proposed approach can be readily extended to incorporate cellular carrier phase measurements, which have been demonstrated to achieve centimeter-level accuracy [18]–[20]. Moreover, if the vehicle is equipped with other navigation sensors, such as lidar or camera, fusing these sensor outputs with cellular pseudorange and carrier phase measurements via the framework discussed in this paper would improve the overall navigation solution. During GNSS unavailability, the proposed framework checks the consistency of pseudorange measurements and calculates the horizontal protection level around the vehicle's estimated position. The framework also detects and excludes a signle faulty cellular LTE signal (i.e., experiencing LOS blockage and high attenuation). The proposed framework assumes the position of cellular towers to be known *a priori*. For the sake of generality, this paper considers three-dimensional (3-D) environments.

This paper is organized as follows. Section II surveys related research on integrity monitoring strategies for ground vehicle navigation and highlights the difference between existing GNSS-based approaches and the proposed approach. Section III describes the extended Kalman filter (EKF)-based navigation framework; including the vehicle's kinematics model, clock errors, cellular pseudorange measurements, estimation of the transmitter's clock biases, and

estimation of the vehicle's states by fusing cellular pseudoranges and IMU measurements. Section IV characterizes cellular pseudorange nominal errors (e.g., short multipath delays) and unmodeled biases (denoted as the fault bias in the sequel) in cellular pseudorange measurements (e.g., LOS signal blockage and high signal attenuation). It also develops a fault detection and exclusion framework and provides protection level calculations. Sections V and VI present simulation and experimental results evaluating the performance of the proposed framework on a ground vehicle navigating in a deep urban environment without GNSS signals. Concluding remarks are given in Section VII.

II. Related Work

Integrity monitoring, in particular RAIM for GNSS signals, have been extensively studied in the literature [33]. In [34], a RAIM method was proposed that provided a detailed theoretical analysis of the integrity under the condition of two-satellite faults. The framework calculated a tighter protection level (PL) for the proposed RAIM by characterizing the maximum slope for every pair of the satellites. The framework considered both GPS and Galileo satellites. In [35], a general formulation for EKF-based RAIM was introduced, which enabled direct integrity risk evaluation. The framework used an EKF-based detection test statistic, which was established as a sum of generalized non-central chi-squared distributed random variables. The proposed method was computationally efficient since the test statistic was recursively updated by adding the current EKF residual contribution to a previously computed weighted norm of past-time residuals. The framework evaluated the sequential nature of Kalman filter (KF) and proposed the batch-processing version of RAIM for KF. In [36], a modified weighted least squared (WLS)-based RAIM was proposed, which focused on a special case of electronic toll collection (ETC) application. The aim of the proposed framework was to decide whether a vehicle has driven through a specific road segment or not. Therefore, The framework tuned the WLS-based RAIM to meet the ETC requirements, due to the fact that as opposed to civil aviation, ETC systems do not require continuity and their RAIM algorithms do not necessarily need to assure a maximum allowed probability of false alarm. In [37], a RAIM algorithm was presented for EKF-based GNSS receivers. The framework proposed a novel method to bound the EKF mean position error. The calculated bounds were used to compute the vertical and the horizontal PLs. The framework surveyed the statistical independency between the EKF position error and the fault test statistic to enable PL computations. The fault profiles were assumed to be the step and ascending ramp functions. In [38], a graph optimization-based framework was employed, which used GPS pseudoranges and a fish-eye camera to simultaneously localize the vehicle as well as the landmarks. Then, the fault mode vector was estimated by analyzing the temporal correlation across the GPS measurement residuals and spatial correlation across the vision intensity residuals. Finally, a Random Sample Consensus (RANSAC)-based technique was proposed to detect and isolate the faults. In [39], a new integrity framework was proposed, which used RAIM for fault detection and exclusion. The framework considered two methods for fault detection and exclusion, based on solution separation (SS) and Chi-squared RAIMs. A new Chi-squared RAIM test statistic was defined and the continuity risk equations for the proposed method were derived. It was shown that there exists a tradeoff between continuity and integrity risk. In [40], a comprehensive overview on GNSS-based integrity for urban transport applications was presented and the differences between the integrity of ground vehicles and the aviation domain were detailed. Then, integrity monitoring approaches for urban environments were categorized in two groups: (i) measurement rejection approach (MRA) and (ii) error characterization approach (ECA). The former provides integrity measure by rejecting the faulty measurements, while the latter computes the PL by characterizing the range measurement errors.

Research developed over decades for GNSS-based RAIM could serve as a starting point for integrity monitoring of cellular-based navigation. However, GNSS methods do not directly apply to cellular-based navigation integrity monitoring due to fundamental differences between cellular and GNSS signals. Although sources of error for GNSS-based navigation have been thoroughly studied [41], they are not fully characterized for cellular SOPs. It is important to note that while some of these errors are not harmful for communication purposes, they severely degrade the navigation performance if they are not modeled and accounted for appropriately. First, due to the low elevation angles at which cellular SOPs are received, these signals experience more multipath compared to GNSS signals, particularly for ground-based receivers in urban canyons [42]. Second, unlike GNSS-based navigation, where the clock error states of GNSS satellites are transmitted in the navigation message, cellular towers do not transmit their clock biases. As such, the clock error states of cellular transmitters must be estimated [43].

III. Model Description

This section presents the dynamics of the vehicle-mounted receiver and cellular SOP clocks, the vehicle's kinematics model, the measurement model of the vehicle-mounted receiver, and the EKF-based navigation framework. The navigation environment is assumed to comprise N_s terrestrial cellular transmitters, denoted $\{S_n\}_{n=1}^{N_s}$. It is assumed that the vehicle knows the location of the cellular transmitters (e.g., from a local or a cloud-hosted database). This database could be generated *a priori* via several approaches, such as radio mapping (e.g., [43], [44]) or satellite images.

A. Vehicle-Mounted Receiver and Cellular SOP Clock Dynamics Model

Since the SOP pseudorange measurement is parameterized by the difference between the receiver's and the SOP's clock biases [45], one only needs to estimate the difference in clock biases and clock drifts. Hence, each SOP will be associated with a state vector $\boldsymbol{\Delta x}_{\mathrm{clk},s_n}$ that consists of the difference

between its clock bias and drift with the clock bias and drift of the vehicle-mounted receiver, i.e.,

$$\boldsymbol{\Delta x}_{\text{clk},s_n} \triangleq \left[c\Delta\delta t_n, c\Delta\dot{\delta} t_n\right]^{\mathsf{T}}, \quad n = 1, \ldots, N_s,$$

where c is the speed of light, $\Delta\delta t_n = \delta t_r - \delta t_{s_n}$ is the difference between the receiver's clock bias δt_r and the n-th SOP's clock bias δt_{s_n}, and $\Delta\dot{\delta} t_n = \dot{\delta} t_r - \dot{\delta} t_{s_n}$ is the difference between the receiver's clock drift $\dot{\delta} t_r$ and the n-th SOP's clock drift $\dot{\delta} t_{s_n}$. Accordingly, the discrete-time dynamic model of the clock error states can be expressed as

$$\boldsymbol{\Delta x}_{\text{clk}}(k+1) = \Phi_{\text{clk}}\boldsymbol{\Delta x}_{\text{clk}}(k) + \boldsymbol{w}_{\text{clk}}(k),$$
$$\Phi_{\text{clk}} \triangleq \begin{bmatrix} \mathbf{F}_{\text{clk}} & \mathbf{0} & \ldots & \mathbf{0} \\ \mathbf{0} & \mathbf{F}_{\text{clk}} & \ldots & \mathbf{0} \\ \vdots & \vdots & \ddots & \vdots \\ \mathbf{0} & \mathbf{0} & \ldots & \mathbf{F}_{\text{clk}} \end{bmatrix}, \quad \mathbf{F}_{\text{clk}} \triangleq \begin{bmatrix} 1 & T \\ 0 & 1 \end{bmatrix}, \tag{1}$$

where $\boldsymbol{\Delta x}_{\text{clk}} = \left[\boldsymbol{\Delta x}_{\text{clk},s_1}^{\mathsf{T}}, \ldots, \boldsymbol{\Delta x}_{\text{clk},s_{N_s}}^{\mathsf{T}}\right]^{\mathsf{T}}$, T is the sampling time, and $\boldsymbol{w}_{\text{clk}}$ is the process noise, which is modeled as a discrete-time zero-mean white random sequence with covariance $\mathbf{Q}_{\text{clk}}$. Additional details of $\mathbf{Q}_{\text{clk}}$ are discussed in [46]–[48].

B. Vehicle Kinematics Model

The vehicle is assumed to be equipped with an IMU and a receiver capable of producing pseudorange measurements to cellular transmitters (e.g., [13], [17], [49], [50]). If the vehicle is equipped with other navigation sensors (e.g., lidar, camera, etc.) the proposed framework could seamlessly integrate the outputs of these sensors to improve the vehicle's navigation solution. The vehicle's state vector $\boldsymbol{x}_r$ is defined as

$$\boldsymbol{x}_r \triangleq \left[{}^{I}_{G}\bar{\boldsymbol{q}}^{\mathsf{T}}, \; {}^{G}\boldsymbol{r}_r^{\mathsf{T}}, \; {}^{G}\dot{\boldsymbol{r}}_r^{\mathsf{T}}, \; \boldsymbol{b}_g^{\mathsf{T}}, \; \boldsymbol{b}_a^{\mathsf{T}}\right]^{\mathsf{T}},$$

where ${}^{F_1}_{F_2}\bar{\boldsymbol{q}}$ is the unit quaternion representing the orientation of frame F_1 with respect to frame F_2; I is the IMU's frame; G is a global frame (e.g., the Earth-centered Earth-fixed (ECEF) frame); ${}^{G}\boldsymbol{r}_r \triangleq \left[{}^{G}x_r, {}^{G}y_r, {}^{G}z_r\right]^{\mathsf{T}}$ and ${}^{G}\dot{\boldsymbol{r}}_r$ are 3-D position and velocity of the vehicle, respectively, expressed in the global frame; and $\boldsymbol{b}_g$ and $\boldsymbol{b}_a$ are the gyroscope and accelerometer biases, respectively. Standard IMU state time update model can be used to propagate the states of the IMU [31], [47], [51], [52].

C. Cellular Pseudorange Measurement Model

After discretization and mild approximations, the pseudorange made by the vehicle-mounted receiver on the n-th cellular transmitter at the k-th time-step can be shown to be [45]

$$z_{s_n}(k) = \left\| {}^{G}\boldsymbol{r}_r(k) - \boldsymbol{r}_{s_n} \right\|_2 + c\Delta\delta t_n + \upsilon_{s_n}(k), \tag{2}$$

where $\boldsymbol{r}_{s_n} \triangleq \left[x_{s_n}, y_{s_n}, z_{s_n}\right]^{\mathsf{T}}$ is the 3-D position of the n-th cellular transmitter and υ_{s_n} is the measurement noise, which is modeled as a discrete-time zero-mean white Gaussian sequence with variance $\sigma_{s_n}^2$.

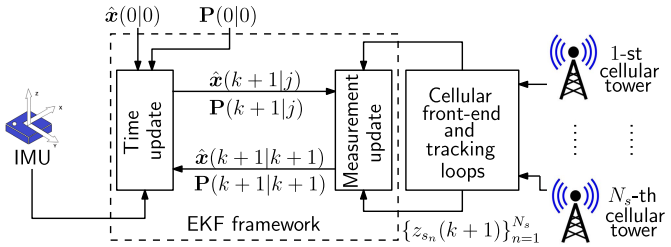

Fig. 2. EKF-based framework for estimating the states.

The vector of pseudorange measurements to all N_s cellular SOPs is given by

$$\boldsymbol{z} = \left[z_{s_1}, \ldots, z_{s_{N_s}}\right]^{\mathsf{T}}.$$

It is assumed that the measurement noise $\left\{\upsilon_{s_n}\right\}_{n=1}^{N_s}$ is independent.

D. Vehicle and Receiver State Estimation

The EKF estimates the state vector $\boldsymbol{x}$ consisting of the vehicle's and the receiver's clock states, i.e. $\boldsymbol{x} \triangleq \left[\boldsymbol{x}_r^{\mathsf{T}}, \boldsymbol{\Delta x}_{\text{clk}}^{\mathsf{T}}\right]^{\mathsf{T}}$. Denote

$$\hat{\boldsymbol{x}}(k|j) \triangleq \left[{}^{I_{k|j}}_{G}\hat{\bar{\boldsymbol{q}}}^{\mathsf{T}}, {}^{G}\hat{\boldsymbol{r}}_r^{\mathsf{T}}(k|j), {}^{G}\hat{\dot{\boldsymbol{r}}}_r^{\mathsf{T}}(k|j), \hat{\boldsymbol{b}}_g^{\mathsf{T}}(k|j), \hat{\boldsymbol{b}}_a^{\mathsf{T}}(k|j), \hat{\boldsymbol{\Delta x}}_{\text{clk}}^{\mathsf{T}}(k|j)\right]^{\mathsf{T}},$$

as the state estimate produced by the EKF at time-step k obtained using all measurements (IMU and cellular pseudorange) from time-step 1 to $j \leq k$ with the associated prediction error covariance $\mathbf{P}(k|j)$. Details of this prediction error model and the process noise can be found in [32], [52], [53].

E. EKF State and Covariance Measurement Update

The EKF state measurement update $\hat{\boldsymbol{x}}(k+1|k+1)$ and associated estimation error covariance $\mathbf{P}(k+1|k+1)$ are computed using standard EKF update equations [47]. Note that the quaternion representation is an over-determined representation of the orientation of a body. Hence, the estimation error covariance associated with the quaternion estimate will always be singular. To avoid singularity, the orientation state is updated according to the quaternion error model [53] (See [54] for more details). The corresponding measurement Jacobian $\mathbf{H}$ is given by $\mathbf{H} \triangleq \begin{bmatrix}\mathbf{H}_{\text{r}_\text{s}} & \mathbf{H}_{\text{clk}}\end{bmatrix}$, where

$$\mathbf{H}_{\text{r}_\text{s}} \triangleq \begin{bmatrix} \mathbf{0}_{1\times 3} & \mathbf{1}_{s_1}^{\mathsf{T}} & \mathbf{0}_{1\times 9} \\ \vdots & \vdots & \vdots \\ \mathbf{0}_{1\times 3} & \mathbf{1}_{s_{N_s}}^{\mathsf{T}} & \mathbf{0}_{1\times 9} \end{bmatrix}, \quad \mathbf{1}_{s_n} \triangleq \frac{{}^{G}\hat{\boldsymbol{r}}_r - \boldsymbol{r}_{s_n}}{\|{}^{G}\hat{\boldsymbol{r}}_r - \boldsymbol{r}_{s_n}\|_2},$$

and

$$\mathbf{H}_{\text{clk}} \triangleq \text{diag}\left[\boldsymbol{h}_{\text{clk},s_1}, \cdots, \boldsymbol{h}_{\text{clk}_{\text{s}},N_{\text{s}}}\right], \quad \boldsymbol{h}_{\text{clk},s_n} \triangleq [1 \quad 0],$$

where diag$(\cdot)$ denotes a diagonal matrix. The measurement noise covariance takes the form $\Sigma_s = \text{diag}\left[\sigma_{s_1}^2, \ldots, \sigma_{s_{N_s}}^2\right]$. The EKF-based estimation framework is illustrated in Fig. 2.

IV. RAIM for Cellular-Based Navigation

RAIM is a technique based on consistency check of redundancy of range measurements. It consists of two main stages:

- **Stage 1:** Performs a fault detection test to detect performance anomalies and to distinguish between fault-free and faulty operations.
- **Stage 2:** Provides a horizontal protection level (HPL), which is the statistical error bound that guarantees that the probability of the absolute position error exceeding a pre-defined threshold is smaller than or equal to the target integrity risk [40].

The target integrity risk refers to the maximum probability with which a receiver is allowed to provide position failures not detected by the integrity monitoring system [55].

This section, first, outlines two sources of cellular pseudorange errors: (i) short multipath delays and (ii) unmodeled biases due to LOS signal blockage. Then, this section describes the steps to compute the HPL for cellular-based navigation.

A. Multipath Characterization

In the presence of multipath, the pseudorange measurement noise for the n-th cellular SOP is inflated to account for the multipath-induced component, denoted m_{b_n}. The proposed multipath model directly contributes in the RAIM system by tuning the EKF measurement covariance matrix, Σ_s, via inflating the noise standard deviation, i.e., $\sigma_{s_n} \rightarrow \alpha.m_{b_n}.\sigma_{s_n}$, where α is an inflation factor design parameter and can be tuned during the GNSS availability period, assuming that the position obtained from GNSS is close to the true position. This in turn affects the protection level calculation, as it will be shown in the next subsection (cf. (5) and (12)). Moreover, this model predicts the measurements with poor quality in the preprocessing stage and increases their error standard deviation, which de-weight them from the measurement set used in the filter calculations.

The multipath component is found through the complex channel impulse response (CIR), which provides information about the time delay and power of each signal path. The CIR can be found using proprietary simulation software (e.g., Wireless InSite). The simulator requires *a priori* knowledge of the environment, including transmitter location, signal characteristics, antenna type, a 3-D building map, and receiver location. This subsection shows how to obtain the multipath component for LTE cellular signals. This methodology can be extended to other cellular signals (e.g., 5G). At each receiver location $p \in \{1, \ldots, P\}$, where P is the total number of simulated receiver locations, the software returns the CIR for the i-th LTE symbol, according to

$$h_{p,i}(t) = \sum_{l=0}^{L-1} a_{p,i}(l)\delta(\tau - \tau_{p,i}(l)), \tag{3}$$

where L is the number of path delays, $a_{p,i}$ corresponds to the complex-valued amplitude, and $\tau_{p,i}$ is the corresponding path delay. Note that path delays greater than the inverse of the signal bandwidth, BW, are excluded from the CIR since their effect will be negligible on the LOS component. The CIR can be used to measure the effect of multipath interference on the receiver's delay-locked loop (DLL), denoted $\chi_{n_p} \triangleq \chi_{1,n_p}(i) + \chi_{2,n_p}(i)$, for $n = 1, \ldots, N_s$, where $\chi_{1,n_p}(i)$ and $\chi_{2,n_p}(i)$ are obtained according to the subcarrier interval T_s, DLL correlator spacing ξ, the number of subcarrier symbols in the LTE pilot signal M, the signal power due to antenna gain and implementation loss A, and the normalized symbol timing error $\tilde{e_\theta}$. Details of the derivation of $\chi_{1,n_p}(i)$ and $\chi_{2,n_p}(i)$ can be found in [56]. The resulting induced multipath component can be calculated according to

$$m_{b_n} = c\frac{\chi_{n_p}}{\kappa}, \quad \kappa \triangleq \frac{4\pi A \cos\left(\frac{\pi}{2M}\right)}{M\left[\sin\left(\frac{\pi}{2M}\right)\right]^3}, \tag{4}$$

where $M \triangleq \left\lfloor \frac{N_r}{6} \right\rfloor$, N_r denotes the number of subcarriers in the received LTE signal, and $\lfloor . \rfloor$ denotes the integer floor function. The multipath component can be computed according to $m_{b_n} \equiv c(\chi_{n_{p^\star}}/\kappa)$, where $p^\star$ indicates the closest simulation point to the vehicle's estimated position. The steps to generate the multipath bias are summarized in Algorithm 1.

Algorithm 1 Steps to Generate the Multipath Bias

Input: N_s, T_s, ξ, M, N_r, A, $\tilde{e_\theta}$, BW
Output: $\{m_{b_n}\}_{n=1}^{N_s}$

```
Retrieve the environment's building map from the database (e.g., BBBike database [57])
Simulate the environment using proprietary software (e.g., Wireless InSite)
Set n = 1
If n ≤ N_s
    Calculate τ_{p,i}, a_{p,i}, and L for each point p in the simulated environment
    Construct the channel CIR using (3)
    If τ_{p,i} > 1/BW
        Exclude τ_{p,i} from the CIR
    Else,
        Find p*, the closest simulation point to the vehicle's estimated position
        Calculate χ_{n_{p*}} using the model detailed in [56]
        Calculate m_{b_n} using (4)
    End if
    Set n = n + 1
Else,
    Output {m_{b_n}}_{n=1}^{N_s}
End
```

B. Unmodeled Biases Due to LOS Signal Blockage

When a high-rise structure completely blocks or significantly attenuates LOS signals from cellular transmitters, the receiver may fail to detect the LOS peak, introducing tens of meters of errors in the estimated position [42]. These unmodeled biases are denoted as the fault bias. In the sequel, the presence of the fault bias in the measurement set is denoted as the faulty operation. In order to distinguish between fault-free and faulty operations, a measurable scalar parameter is

defined that provides information about pseudorange measurement errors. This parameter, called a test statistic φ, is a random variable with a known distribution. In this paper, the normalized innovation squared (NIS) is used for generating the test statistic according to

$$\varphi(k+1) = \boldsymbol{\nu}^{\mathsf{T}}(k+1)\mathbf{S}^{-1}(k+1)\boldsymbol{\nu}(k+1),$$

where the innovation vector $\boldsymbol{\nu}$ and its corresponding covariance matrix $\mathbf{S}$ are computed from

$$\begin{aligned}\boldsymbol{\nu}(k+1) &= \boldsymbol{z}(k+1) - \hat{\boldsymbol{z}}(k+1|k) \\ \mathbf{S}(k+1) &= \mathbf{H}(k+1)\mathbf{P}(k+1|k)\mathbf{H}^{\mathsf{T}}(k+1) + \Sigma_s.\end{aligned} \tag{5}$$

The NIS-based test statistics follows a chi-squared distribution in fault-free operation and a non-central chi-squared distribution in faulty operation [37]. Both distributions under fault-free and faulty operations have the same degrees of freedom $d = N_s$. The non-centrality parameter in faulty operation is given by

$$\lambda(k+1) = \boldsymbol{u}_i^{\mathsf{T}}(k+1)\mathbf{S}^{-1}(k+1)\boldsymbol{u}_i(k+1),$$

where vector $\boldsymbol{u}_i \triangleq [0, \ldots, 0, b_i, 0, \ldots, 0]^{\mathsf{T}}$ indicates the faulty cellular transmitter along with the magnitude of the bias in the pseudorange measurement drawn from the faulty transmitter (i.e., b_i). It is worth mentioning that the fault vector $\boldsymbol{u}_i$ aims to detect only one large fault bias due to LOS blockage, which is induced into the measurements. For complicated wireless environments with multiple faults, more sophisticated methods must be employed. Formulating other types of RAIM for SOP-based navigation has been investigated in other work, e.g., see [58] for GPS-SOP RAIM. Here, the fault detection is achieved by comparing the test statistic against the detection threshold T_h, i.e.,

$$\begin{aligned}&\varphi(k+1) \leq T_h : \text{no fault detected,} \\ &\varphi(k+1) > T_h : \text{fault detected.}\end{aligned}$$

A Neyman-Pearson approach is taken to obtain T_h given a desired probability of false alarm, P_{FA}, under a fault-free operation according to

$$P_{\text{FA}} = \int_{T_h}^{\infty} f_{\chi^2_d}(\tau)d\tau, \tag{6}$$

where $f_{\chi^2_d}$ represents the probability density function (pdf) of the chi-squared distribution with d degrees of freedom. Once a desired P_{FA} is fixed, T_h can be evaluated numerically from (6) or a chi-squared cumulative density function (cdf) table.

C. Horizontal Protection Level

For each estimated position, RAIM provides HPL, a circular area centered at the user's real position, which is assured to contain the estimated position with a probability equal or higher than $1 - P_{\text{MD}}$, where P_{MD} is a probability of missed detection [36]. The decision of alert is done by comparing the HPL and a specified horizontal alert limit (HAL), which is the largest position error allowable for safe operation. The non-centrality parameter of the chi-squared distribution under faulty operation that results in a missed detection rate P_{MD} is defined by λ_{min}. Given a specified P_{MD} as a design parameter and T_h obtained from (6), λ_{min} is computed according to

$$P_{\text{MD}} = \int_0^{T_h} f_{\chi^2_d,\lambda_{min}}(\tau)d\tau, \tag{7}$$

where $f_{\chi^2_d,\lambda_{min}}$ represents the pdf of the non-central chi-squared distribution with d degrees of freedom and non-centrality λ_{min} parameter.

Next, a parameter called slope_i is introduced to couple the effect of the fault in the i-th measurement and the test statistic. To find a mathematical derivation for slope_i, first, the faulty measurement vector is modeled as

$$\boldsymbol{z}_{\boldsymbol{u}_i}(k+1) \triangleq \boldsymbol{z}(k+1) + \boldsymbol{u}_i(k+1). \tag{8}$$

The bias in the measurement leads to an additive bias in the error states, i.e.,

$$\hat{\boldsymbol{x}}_{\boldsymbol{u}_i}(k+1|k+1) \triangleq \hat{\boldsymbol{x}}(k+1|k+1) + \boldsymbol{\Delta x}_{err,i}(k+1). \tag{9}$$

Note that the additive bias in the error states $\boldsymbol{\Delta x}_{err,i}$ will be propagated in the next time-update, according to

$$\boldsymbol{\Delta x}_{err,i}(k+1) = \mathbf{F}(k)\boldsymbol{\Delta x}_{err,i}(k). \tag{10}$$

The effect of the measurement fault on the state estimate can be calculated using the EKF measurement update equation under faulty condition, according to

$$\begin{aligned}\hat{\boldsymbol{x}}_{\boldsymbol{u}_i}(k+1|k+1) &= \hat{\boldsymbol{x}}_{\boldsymbol{u}_i}(k+1|k) \\ &\quad + \mathbf{K}(k+1)[\boldsymbol{z}_{\boldsymbol{u}_i}(k+1) - \hat{\boldsymbol{z}}_{\boldsymbol{u}_i}(k+1|k)],\end{aligned} \tag{11}$$

where $\mathbf{K}$ is the Kalman filter gain, and is given by

$$\mathbf{K}(k+1) = \mathbf{P}(k+1|k)\mathbf{H}^{\mathsf{T}}(k+1)\mathbf{S}^{-1}(k+1). \tag{12}$$

Substituting (8)–(10) into (11) leads to

$$\begin{aligned}&\hat{\boldsymbol{x}}(k+1|k+1) + \boldsymbol{\Delta x}_{err,i}(k+1) \\ &= \hat{\boldsymbol{x}}(k+1|k) + \mathbf{F}(k)\boldsymbol{\Delta x}_{err,i}(k) \\ &\quad + \mathbf{K}(k+1)[\boldsymbol{z}(k+1) + \boldsymbol{u}_i(k+1) \\ &\quad - \hat{\boldsymbol{z}}_{\boldsymbol{u}_i}(k+1|k)].\end{aligned} \tag{13}$$

A first-order EKF measurement update equation can be used to approximate $\hat{\boldsymbol{z}}_{\boldsymbol{u}_i}(k+1|k)$ [47], [59] according to

$$\begin{aligned}\hat{\boldsymbol{z}}_{\boldsymbol{u}_i}(k+1|k) &\approx \mathbf{H}(k+1)\hat{\boldsymbol{x}}_{\boldsymbol{u}_i}(k+1|k+1) \\ &= \mathbf{H}(k+1)\left[\hat{\boldsymbol{x}}(k+1|k+1) + \boldsymbol{\Delta x}_{err,i}(k+1)\right].\end{aligned} \tag{14}$$

Substituting (10) and (14) into (13) approximates $\boldsymbol{\Delta x}_{err,i}(k+1)$ according to

$$\begin{aligned}\boldsymbol{\Delta x}_{err,i}(k+1) &\approx \mathbf{F}(k)\boldsymbol{\Delta x}_{err,i}(k) \\ &\quad + \mathbf{K}(k+1)\boldsymbol{u}_i(k+1) \\ &\quad - \mathbf{K}(k+1)\mathbf{H}(k+1)\mathbf{F}(k)\boldsymbol{\Delta x}_{err,i}(k) \\ &= [\mathbf{I} - \mathbf{K}(k+1)\mathbf{H}(k+1)]\mathbf{F}(k)\boldsymbol{\Delta x}_{err,i}(k) \\ &\quad + \mathbf{K}(k+1)\boldsymbol{u}_i(k+1).\end{aligned} \tag{15}$$

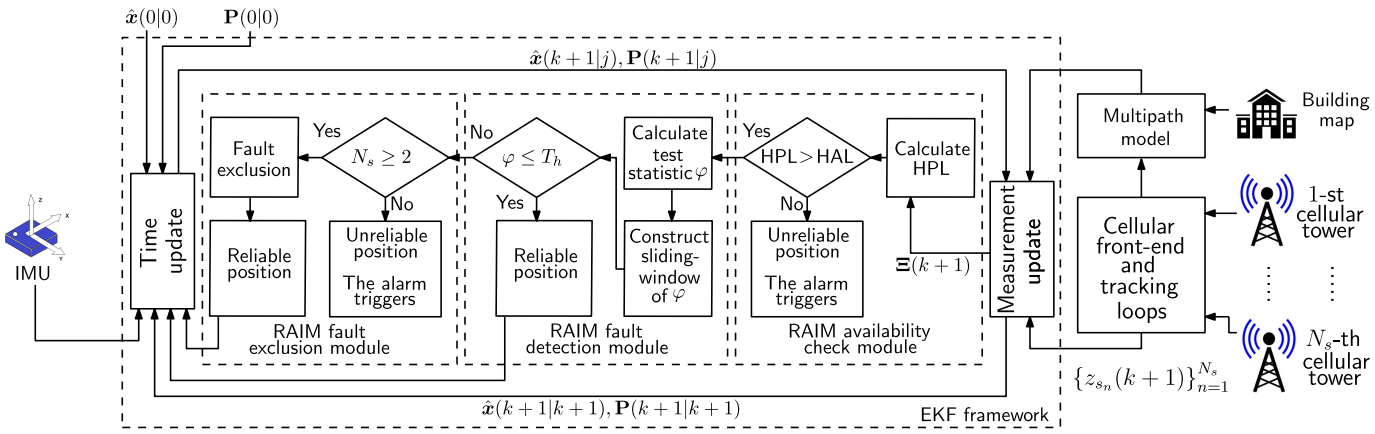

Fig. 3. Block diagram of the proposed framework, updated from Fig. 2 showing a flowchart summary of the proposed cellular SOP-based RAIM. The proposed method consists of five main parts: EKF calculations, error characterization, availability check, fault detection, and fault exclusion. In order to avoid false alarms caused by noise sparks of φ, instead of switching between faulty operation and fault-free operation based upon a single φ, a sliding window of φ values was considered. Hence, the faulty operation is declared if and only if all φ elements inside a sliding window exceed the threshold.

Replacing $[\mathbf{I}-\mathbf{K}(k+1)\mathbf{H}(k+1)]\mathbf{F}(k)$ with $\Psi(k+1)$, (15) may be expressed in a recursive form according to

$$\begin{aligned}\boldsymbol{\Delta x}_{err,i}(k+1) = {} & \Psi(2)\ldots\Psi(k+1)\mathbf{K}(1)\boldsymbol{u}_i(1) \\ & + \Psi(3)\ldots\Psi(k+1)\mathbf{K}(2)\boldsymbol{u}_i(2) \\ & + \Psi(4)\ldots\Psi(k+1)\mathbf{K}(3)\boldsymbol{u}_i(3) \\ & \vdots \\ & + \mathbf{K}(k+1)\boldsymbol{u}_i(k+1). \end{aligned} \tag{16}$$

The navigation system is assumed to be stable, therefore, $\Psi(i)\Psi(i+1)\ldots\Psi(i+k) \approx 0$ for large values of k. As a result, $\boldsymbol{\Delta x}_{err,i}(k+1)$ only depends on the last N_{eff} time-steps. In cellular-based navigation frameworks, the update sampling time is high (e.g., 100 Hz for cellular LTE signals). Moreover, unlike GNSS satellites, cellular transmitters are spatially-stationary. Due to the large mass and inertia of the vehicle, the relative position of the vehicle with respect to cellular transmitters do not change significantly in the last N_{eff} time-steps. Therefore, without loss of generality, it is possible to assume that $\boldsymbol{u}_i(k+1-N_{\text{eff}}) \approx \boldsymbol{u}_i(k+2-N_{\text{eff}}) \approx \ldots \approx \boldsymbol{u}_i(k+1)$. Hence, $\boldsymbol{\Delta x}_{err,i}(k+1)$ can be approximated with

$$\boldsymbol{\Delta x}_{err,i}(k+1) \approx \Xi(k+1)\boldsymbol{u}_i(k+1),$$

where

$$\Xi(k+1) = \sum_{i=1}^{k+1}\Big(\prod_{j=i+1}^{k+1}\Psi(j)\Big)\mathbf{K}(i).$$

The recursive equation of $\Xi(k+1)$ becomes

$$\begin{aligned}\Xi(k+1) &= \Psi(k+1)\Xi(k) + \mathbf{K}(k+1) \\ \Xi(1) &= \mathbf{K}(1).\end{aligned}$$

Since the projection of the fault in the measurement should be considered in the horizontal plane (i.e., e- and n-directions in the East, North, UP (ENU) frame), the fourth, fifth, and sixth rows of $\Xi(k+1)$ (i.e., x-, y-, and z- directions in the global frame) is used to construct the slope_i. Subsequently, slope_i is expressed according to

$$\begin{aligned}\text{slope}_i(k+1) &= \frac{\xi_i(k+1)}{\sqrt{(\mathbf{S}^{-1}(k+1))_{i,i}}}, \\ \xi_i(k+1) &= \sqrt{[(\Xi_{\text{ENU}}(k+1))_{1,i}]^2 + [[(\Xi_{\text{ENU}}(k+1))_{2,i}]^2},\end{aligned} \tag{17}$$

where $(\mathbf{A})_{i,j}$ indicates the element of the i-th row and the j-th column of matrix $\mathbf{A}$ and Ξ_{ENU} is the projection of Ξ from the global frame into the ENU frame. The HPL is calculated as the projection in the position domain of the pseudorange measurement bias that generates a non-centrality parameter equal to λ_{min} in the cellular transmitter with the maximum slope [55], i.e.,

$$\text{HPL}(k+1) = \text{slope}_{max}(k+1)\sqrt{\lambda_{min}},$$

where

$$\text{slope}_{max}(k+1) = \max_i\{\text{slope}_i(k+1)\}, \quad i = 1, \ldots, N_s.$$

Remark: The parameter N_{eff} can be determined by setting a threshold on the decrease rate of the terms of (16). Similar to the method presented in [37], this can be achieved by finding the minimum N_{eff} that holds the inequality of $\max\{\lambda_i[\mathbf{Y}(N_{\text{eff}})]\} < thr_{N_{\text{eff}}}$, where the $\max(\cdot)$ operator is performed over all eigenvalues λ_i of $\mathbf{Y}(N_{\text{eff}})$ defined as

$$\mathbf{Y}(N_{\text{eff}}) \triangleq \Big[\prod_{j=k}^{k+N_{\text{eff}}}\Psi(j)\mathbf{K}(k-1)\Big]\Big[\prod_{j=k}^{k+N_{\text{eff}}}\Psi(j)\mathbf{K}(k-1)\Big]^{\mathsf{T}}.$$

Tuning N_{eff} can be performed adaptively, i.e., in each time-step, the N_{eff} is increased to the point where the above inequality holds. The updated N_{eff}, then, will be used in the next time-step. An example of max eigenvalues versus N_{eff} is shown in Fig. 4. Here, for $thr_{N_{\text{eff}}} = 1\times10^{-20}$, $N_{\text{eff}} = 13$ can be used.

The procedure of fault exclusion has been extensively studied in the literature. In [28], a simple, yet effective process

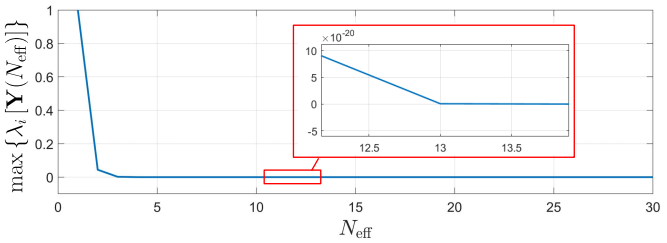

Fig. 4. An example of $\mathbf{Y}(N_{\text{eff}})$ versus N_{eff}.

to exclude single faults was described. A more comprehensive fault exclusion procedure was introduced in [60], which was able to detect and exclude multiple faults at each time-step. Moreover, analysis of navigation solution integrity after performing the exclusion was detailed in [60]. In contrast to [28] and [60], where the exclusion process started from all-in-view subset, [61] proposed an exclusion technique based on the RANSAC algorithm by evaluating subsets that includes only 4 satellites and testing the consistency of the satellites outside of the subset. This framework was also able to detect multiple failures and was shown to be as effective as traditional exclusion techniques. Since all the aforementioned techniques uses the measurement residuals to test the consistency of the pseudoranges within a subset of the satellites, they are applicable in the cellular SOP-based RAIM as well. In this paper, the algorithm described in [28] was employed, where a single fault was assumed, and the fault exclusion was performed by constructing N_s subsets of $N_s - 1$ pseudorange measurements, each of which excludes one pseudorange measurement at a time. This exclusion procedure can be justified in the sense that applying the fault detection module to each subgroup will detect a fault in all of them except in the one that already excluded the faulty measurement. Note that this fault exclusion needs at least two redundant range measurements and it is available when fault detection is available for each subgroup. A thorough analysis of the unavailability rate of this fault exclusion scheme was provided in Appendix E of [28]. Fig. 3 demonstrates the EKF-based estimation framework along with a flowchart summary of the proposed cellular-based RAIM.

Finally, the receiver operating characteristic (ROC) curves for the proposed fault detection and exclusion method are shown in Fig. 5, for low and high values of number of transmitters ($N_s \in \{4, 15\}$) and low and high values of λ_{min} ($\lambda_{min} \in \{5, 15\}$). The ROC curve evaluates the detection performance of a fault detection method by plotting the probability of false alarm (horizontal-axis) versus the probability of detection (vertical-axis). For comparison purposes, the proposed method's ROC curves are plotted against the ROC curves of a fault detection method which used a least squares (LS) filter. As can be seen from Fig. 5, while both the EKF-based and LS-based fault detection methods have a comparable performance for large number of transmitters, the EKF-based fault detection method is more desirable, as it can detect faults whenever the number of transmitters is low. A comprehensive analysis of these two fault detection methods for GNSS can be found in [62].

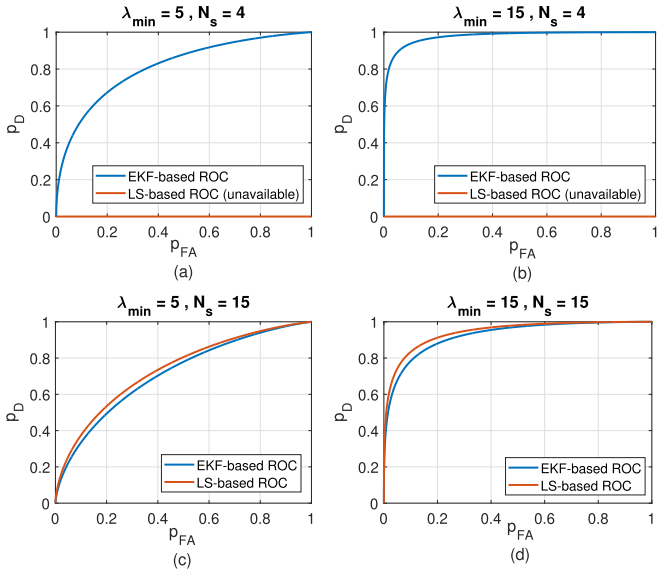

Fig. 5. ROC curves for the EKF-based and LS-based fault detection methods. It can be seen that both methods have a comparable performance for large number of transmitters. However, the EKF-based method outperforms the LS-based method in the case of low number of transmitters ($N_s = 4$), as the LS-based method is incapable of detecting faults due to not having sufficient degrees of freedom.

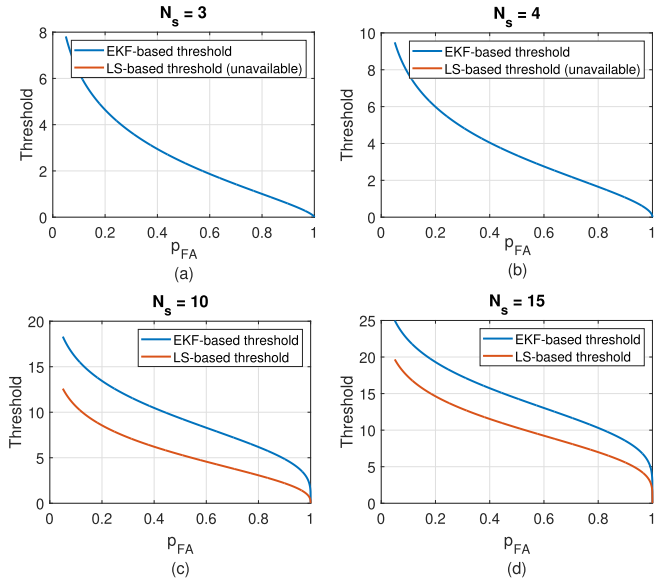

Fig. 6. The threshold for LS-based and EKF-based test statistics for $N_s = 3$, 4, 10, and 15 transmitters. As can be seen, the LS-based threshold for $N_s = 3$ and $N_s = 4$ is unavailable due to not having sufficient degrees of freedom.

The test statistic threshold for both LS-based and EKF-based fault detection methods is shown in Fig. 6 for low and high values of N_s and for P_{FA} ranging from 0.05 to 1. Note that the LS-based method is not able to detect faults for $N_s = 3$ and $N_s = 4$ due to not having sufficient degrees of freedom.

V. Simulation Results

A simulation test was performed to evaluate the performance of the proposed method described in Section IV. In this

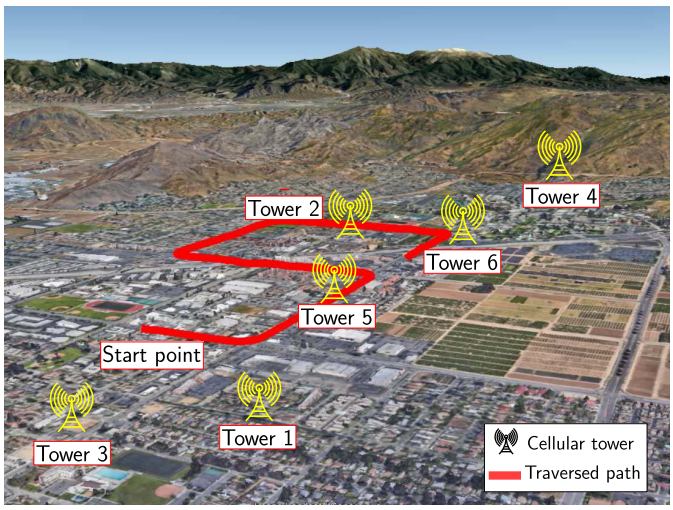

Fig. 7. The simulation environment layout, trajectory traversed by the vehicle, and position of cellular towers.

simulation, a ground vehicle was assumed to be equipped with a consumer grade IMU and a receiver capable of producing pseudorange observation on the ambient cellular towers. The vehicle was assumed to traverse 4 km in an urban environment (downtown Riverside, California, USA) comprising six cellular LTE transmitters, whose locations were chosen according to real LTE towers in that environment. The simulation settings are given in Table I. In previous work [15], the ranging performance of cellular measurements was characterized from an extensive wardriving campaign collected with a ground vehicle in different environments: open sky, urban, and deep urban. It was shown that the cellular pseudorange measurement error standard deviation ranges from 0.1 m in open sky to 2.7 m in urban environments. This justifies the choice of $\{\sigma^2_{s_n}\}_{n=1}^{N_s} = 4\,\mathrm{m}^2$ in Table I. Fig. 7 illustrates the simulation environment layout, the trajectory traversed by the ground vehicle, and the position of cellular towers.

The model presented in Subsection IV-A was used to simulate the effect of multipath on the measurements using the multipath parameters given in Table I. Fig. 8 shows the simulated induced multipath biases $\{m_{b_n}\}_{n=1}^{6}$ obtained from Algorithm 1 for all six transmitters. Fig. 8 demonstrates regions where the multipath component exceeds thresholds shown in the figure's colorbar. Note that the multipath error was calculated at equally spaced points (10 meter spacing). The building map was retrieved from BBBike database [57]. The buildings were assumed to be concrete with heights of 25 meters. These biases were added into the pseudorange measurements drawn from the six cellular towers. Four different faults were introduced into the pseudorange drawn from cellular tower 6, starting at $t = 100$ s. It is important to mention that although the NIS-based test statistic was shown to be effective to detect ramp faults with large increasing rates, it is not robust in detecting slowly growing faults with small initial amplitudes. Therefore, detecting slowly growing faults are not considered in this simulation test and the simulations are limited to ramps with small initial value, but, fairly high growth rate. Here, the ramp faults were defined with an initial value of 0 m and a growth rate of 0.05 m/T. Setting $T = 0.01$ s, the ramp faults were grown over the period of 3 s and 6 s, for the faults with maximum of 15 m and 20 m, respectively. Fig. 9 shows the

TABLE I
SIMULATION SETTINGS

Parameter	Definition	Value
P_{FA}	False alarm probability	5×10^{-4}
P_{MD}	Missed detection probability	5×10^{-4}
${}^{G}\boldsymbol{r}_r(0)$	Vehicle initial position (ENU)	$[0, 0, 0]$ m
N_s	Number of transmitters	6
T	Sampling time	0.01 s
α	Inflation factor	1
$\boldsymbol{b}_6$	Fault magnitude	15 m and 30 m
	Fault type	Ramp, Step
	Ramp fault grow rate	0.05 m/(time-step)
$\{\sigma^2_{s_n}\}_{n=1}^{N_s}$	measurement variance	4 m^2 [15]
$\boldsymbol{r}_{s_n}$	Tower positions (ENU)	$[718, -5481, -115;$ $-587, -5700, -59;$ $601, -4775, -77;$ $563, -6448, -103;$ $2170, -5902, -98;$ $-1747, -7396, -131]$ m
T_s	Subcarrier interval	3.2552×10^{-8} s
$\tau_{p,i}$	Channel path delay	An output of Wireless InSite
$a_{p,i}$	Channel path amplitude	An output of Wireless InSite
ξ	DLL correlator spacing	0.5
L	Number of path delays	An output of Wireless InSite
M	Number of subcarrier symbols in the LTE pilot signal	200
N_r	Number of subcarrier symbols in the received LTE signal	1200
A	Antenna gain and implementation loss	1
$\tilde{\epsilon}_\theta$	Normalized symbol timing error	0
	IMU angular rate measurement noise covariance	$2.9387 \times 10^{-9}\mathbf{I}_{3\times3}$ (rad/ s)^2
	IMU specific force measurement noise covariance	$4.217 \times 10^{-13}\mathbf{I}_{3\times3}$ (m/ s^2)^2
	IMU gyroscope bias noise covariance	$1 \times 10^{-10}\mathbf{I}_{3\times3}$ (rad/ s^2)^2
	IMU accelerometer bias noise covariance	$1 \times 10^{-10}\mathbf{I}_{3\times3}$ (m/ s^3)^2
	Clock bias process noise power spectral density of transmitters	4×10^{-20} s
	Clock drift process noise power spectral density of transmitters	7.89×10^{-22} 1/s
	Clock bias process noise power spectral density of the receiver	4.7×10^{-20} s
	Clock drift process noise power spectral density of the receiver	7.5×10^{-20} 1/s

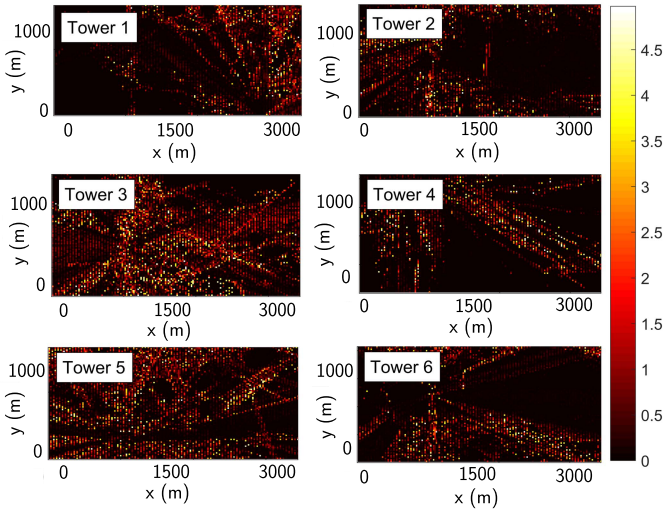

Fig. 8. The simulated induced multipath bias for all cellular towers obtained from (4). These biases were introduced into the pseudorange measurements drawn from cellular tower 1–6. In this figure, x-axis and y-axis represent East and North in the ENU coordinate frame, respectively.

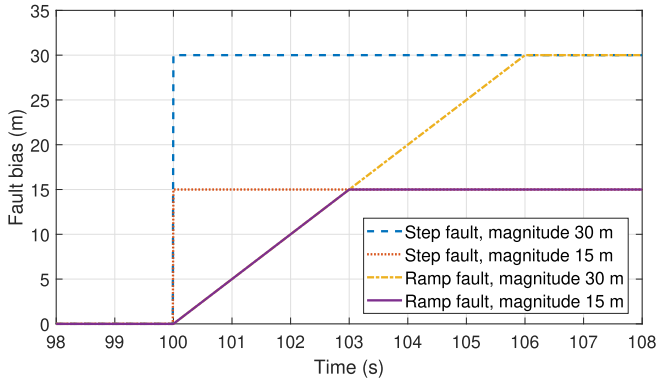

Fig. 9. The corresponding fault profiles for the generated step and ramp faults in the simulation. The maximum magnitude of the faults were set to 15 m and 30 m. The initial values were set to 0 m and the growth rate of the ramp faults were set to 5 m/s.

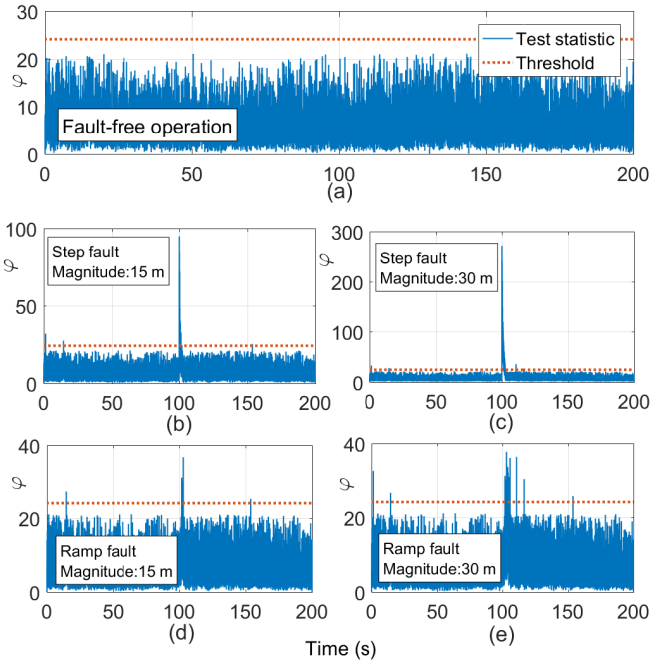

Fig. 10. The resulting test statistic for the faults with ramp and step profile. As can be seen, the framework has a similar performance to detect faults with a step and ramp profiles.

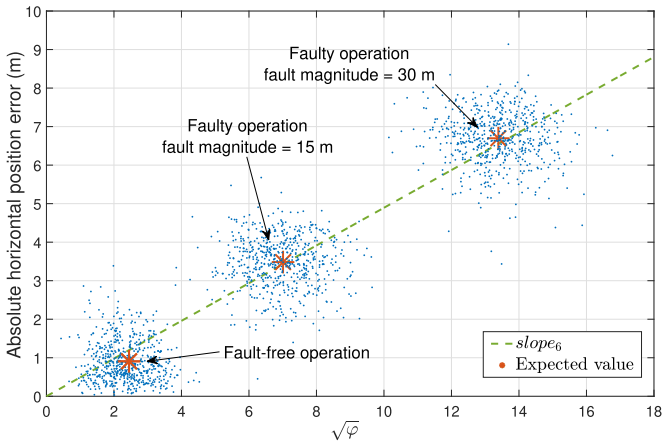

Fig. 11. Simulation results for a comparison between the analytically calculated slope using the proposed framework and the simulated one for fault-free and faulty operations. It is evident from this figure that slope obtained from (17) follows its true value.

corresponding fault profiles for the generated step and ramp faults in this simulation.

The fault detection approach formulated in Subsection IV-B was executed on the simulated data. Fig. 10 shows the fault detection test obtained by comparing the test statistic φ against the detection threshold T_h for (a) fault-free operation and (b)–(e) faulty operations. As shown in Fig. 10, the resulting test statistic has lower values in the ramp faults compared to the step faults. This emphasizes the fact that detecting and excluding the faults with ramp profile is harder compared to the faults with step profile. However, the framework has a similar performance in detecting faults with both step and ramp profiles.

In Fig. 11, the proposed slope as calculated by (17) is given by the dashed green line, together with simulated data. In this figure, slope is associated with the sixth transmitter. The simulated data consist of 600 measurements at a single epoch are shown by blue dots. Along the horizontal axis, the squared test statistic and along the vertical axis the absolute horizontal position error are given. The expected value is given by the red cross. The simulations were run for 3 scenarios: fault-free operation and two faulty operations, where a bias of 15 m and 30 m was given to the measurement drawn from the sixth transmitter. In this figure, it is clearly visible that the expected value travels along the slope computed from (17). This shows that the proposed method correctly calculates the mapping between the error in the test statistic domain and the error in the position domain in order to construct the HPL.

For comparative analyses, next, the performance of the proposed framework is compared with the method presented in [15]. In [15], a stationary agent, referred to as the base,

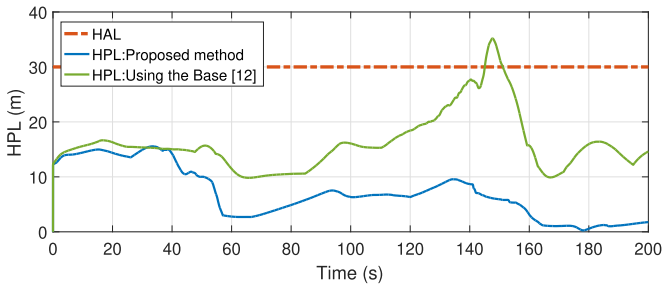

Fig. 12. A comparison between the obtained HPL using the proposed method, versus the HPL obtained from navigation framework presented in [15], where a base was employed to estimate the clock bias states of the cellular transmitters and to share these estimates with the navigating vehicle.

was employed to estimate the clock bias states of the cellular transmitters and to share these estimates with the navigating vehicle. Similar to the previous simulation run, the induced multipath biases shown in Fig. 8 were added into the pseudo-range measurements. Fig. 12 shows the comparison between the HPL obtained from the proposed method, versus the HPL obtained from the navigation framework presented in [15]. It is evident that using the proposed radio SLAM-based approach archives tighter HPL. This is due to the fact that the base suffers from clock model mismatch, which introduces an error into the clock bias estimates.

VI. Experimental Results

Two field experiments were conducted to validate the proposed framework on a ground vehicle navigating in an urban environment: downtown Riverside, California, USA. This section presents the software and hardware used in this experiment along with the experimental results.

A. Experimental Software and Hardware Setup and Scenario Description

A ground vehicle was equipped with a sophisticated ground truth system, which includes:

- an integrated Septentrio AsteRx-i V GNSS-IMU system that has a tactical grade IMU [63]
- a dual-antenna, multi-frequency GNSS receiver
- a Vectornav VN-100 micro electromechanical systems (MEMS) IMU
- a post-processing software development kit (PP-SDK) to process carrier phase observables to produce a carrier phase-based navigation solution

This integrated GNSS-IMU real-time kinematic (RTK) system [63] utilized GPS and GLONASS satellites and was used to produce the ground truth results with which the proposed navigation framework was compared. The AsteRx-i V allows access to the raw measurements from this IMU, which was used for the time update of the orientation, position, and velocity as described in Section III. During the course of the experiment, there was a sufficient number of trackable GNSS satellites, which were used to aid the INS. It is worth noting that one could obtain a "better" ground truth trajectory (i.e., with a closer match with the true vehicle trajectory) via a more sophisticated sensor suite setup by utilizing vehicle encoder and visual/lidar SLAM. Nevertheless, the vehicle used in these experiments did not utilize encoders, cameras, or lidar.

The vehicle was also equipped with two cellular antennas to acquire and track signals from nearby cellular LTE towers. The LTE antennas used for the experiment were consumer-grade 800/1900 MHz cellular antennas. The signals were simultaneously down-mixed and synchronously sampled via a National Instruments (NI) dual-channel universal software radio peripheral (USRP)–2954R, driven by a GPS-disciplined oscillator (GSPDO).

The clock bias and drift process noise power spectral densities of the receiver were set to be 1.3×10^{-22} s and 7.89×10^{-25} 1/s respectively, since the 2954R USRP was equipped with oven-controlled crystal oscillator (OCXO). The receiver was tuned to carrier frequencies of 1955 MHz and 739 MHz, which are channels allocated for the U.S. cellular provider AT&T. Samples of the received signals were stored for off-line post-processing. The Multichannel Adaptive TRansceiver Information eXtractor (MATRIX) software-defined receiver (SDR) developed in [14] was used to produce LTE pseudor-anges.

During the period of GNSS availability, the initial estimates of the vehicle's orientation ${}^{I}_{G}\hat{\bar{\boldsymbol{q}}}(0|-1)$, position ${}^{G}\hat{\boldsymbol{r}}_r(0|-1)$, and velocity ${}^{G}\hat{\dot{\boldsymbol{r}}}_r(0|-1)$, and their covariances were obtained using the output of the GNSS-IMU system. The gyroscope's and accelerometer's biases; $\hat{\boldsymbol{b}}_g(0|-1)$ and $\hat{\boldsymbol{b}}_a(0|-1)$, respectively; were obtained by taking the mean of 5 seconds of IMU data, when the receiver was stationary. Since the vehicle had initial access to GNSS signals, the initial values of the clock error states were obtained. The initial uncertainties associated with these state estimates were set to $\mathbf{P}_{{}^{I}_{G}\bar{\boldsymbol{q}}}(0|-1) = (1\times10^{-3})\mathbf{I}_{3\times3}$, $\mathbf{P}_{{}^{G}\boldsymbol{r}_r}(0|-1) = \text{diag}\,[10, 10, 0.5]$, $\mathbf{P}_{{}^{G}\dot{\boldsymbol{r}}_r}(0|-1) = \text{diag}\,[1, 1, 0.1]$, $\mathbf{P}_{\boldsymbol{b}_g}(0|-1) = \left(3.75\times10^{-9}\right)\mathbf{I}_{3\times3}$, and $\mathbf{P}_{\boldsymbol{b}_a}(0|-1) = \left(9.6\times10^{-5}\right)\mathbf{I}_{3\times3}$, where $\mathbf{I}_{l\times l}$ is a l-dimensional identity matrix. During this test, P_{FA} and P_{MD} were set to 0.001 and 0.0005, respectively, and HAL was set to 20 m. The measurement noise standard deviations were calculated empirically, while the vehicle had access to GNSS signals. The measurement noise standard deviations for towers 1 through 5 were calculated to be 1.66, 4.26, 2.67, 3.52, 1.33 m, respectively.

Over the course of the experiment the receiver was listening to 5 LTE towers. The ground vehicle traversed a trajectory of 825 m. Fig. 13 illustrates the experimental hardware setups, experimental environment, and the traversed trajectory along with the location of the base and the LTE towers.

The navigation solution was obtained using three different methods:

- **Method 1:** Without using the fault exclusion and without using the multipath model
- **Method 2:** With using the fault exclusion and without using the multipath model
- **Method 3 (proposed):** With using the fault exclusion and with using the multipath model

The difference between **Method 2** and **Method 3** is that the former only uses the fault detection and exclusion presented

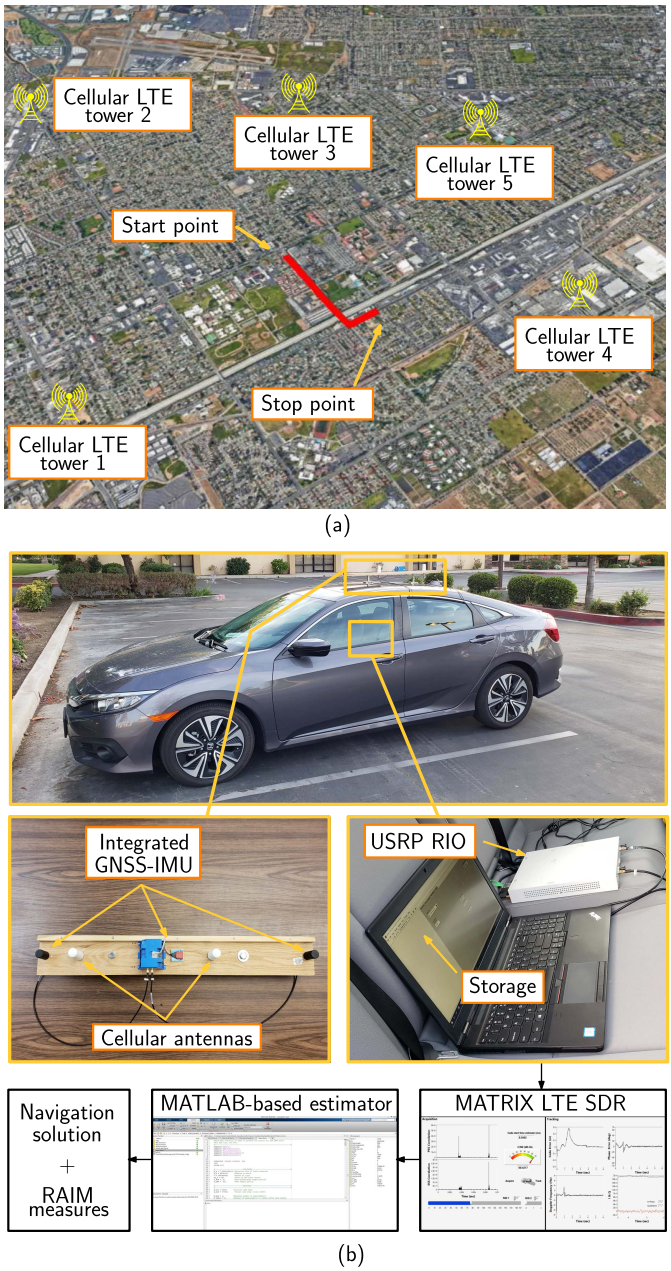

Fig. 13. Experimental software and hardware setup, experimental environment, and the traversed trajectory along with the position of the base and the cellular towers. (a) The experiment environment layout, the eNodeBs positions, and the start point. Image: Google Earth. (b) The ground vehicle that was equipped with an integrated AsteRx-i GNSS-IMU sensor, cellular antennas, and a USRP. The vehicle traversed 825 m in an urban area (downtown Riverside, California, USA) collecting GNSS, IMU measurements, and cellular LTE signals from five cellular towers.

in Subsection IV-B, while the latter not only uses the fault detection and exclusion, but also uses the multipath model presented in Subsection IV-A to dynamically tune the measurement covariance matrix. Subsection VI-C presents the comparison between the navigation solutions obtained from each method.

B. Environment 1 Experimental Results

The first experimental test was conducted in an urban environment: downtown Riverside, California, USA. The fault detection and exclusion were performed throughout the experimental test. Fig. 14 shows the fault detection test, which compares the test statistic φ against the detection threshold T_h. It can be seen that at $t = 40$ s, the threshold is exceeded; therefore, the test is not declared successful (see the red circle in Fig. 14 (a)). This implies that at least one of the measurements was faulty and its contribution to the test statistic was significant enough for the test to fail. The fault exclusion technique indicated that the faulty measurement was the pseudorange drawn from the second cellular LTE tower. In post processing, the second measurement was excluded.

Fig. 14 (b)–(c) shows the resulting position estimation error and corresponding $\pm 2\sigma$ bounds with and without using the proposed fault exclusion. As can be seen, fault exclusion results in improvement in the x- and y-direction position RMSE. Fig. 14 (d)–(e) shows the estimated clock error states for the first SOP (i.e., the difference between the clock bias and clock drift of the receiver and first SOP) and corresponding variances. It can be seen that using the proposed algorithm the estimated variances remain stable in the course of the experiment. Since the actual receiver's clock error states are not available, it is impossible to show the estimation errors. Finally, Fig. 14 (f)–(g) demonstrate the resulting estimation trajectories and corresponding variances for the IMU's gyroscope and accelerometer biases. It is worth noting that since the SOP transmitters' altitude suffers from geometric diversity, the estimation in the z-direction will have high error. For a ground vehicle, this can be readily solved by incorporating map data [64], [65]. For a UAV, this can be alleviated with the aid of other sensors such as an altimeter [20]. Fig. 14 is limited to 2-D results.

Fig. 15 shows the resulting velocity estimation error with and without using the proposed fault exclusion in the $x-$ and $y-$directions. As expected, the proposed framework not only impacts the position estimation, but also improves the velocity estimation.

Fig. 16 illustrates the HPL and HAL. In contrast to weighted least-square (WLS)-based RAIM [36] where the HPL does not depend on the current measurements and can be predicted according to the expected satellite/user geometry, the HPL in the proposed RAIM method depends on both the current states and measurements. Therefore, it must be calculated at each time-step. As can be seen, over the course of the experiment, HPL does not exceed HAL. Subsequently, RAIM was available throughout the experiment, which means that RAIM was able to detect the presence of the faults within the required P_{MD}.

Table II compares the navigation performance of Methods 1–3. The results demonstrated an RMSE of 11.08 m over the 825 m trajectory without measurement exclusion and RMSE of 5.82 m with measurement exclusion. Therefore, incorporating the proposed algorithm, reduced the position RMSE by 66% from the RMSE obtained by a navigation solution without fault exclusion. Moreover, the results demonstrated that the standard deviation of the estimation error without measurement exclusion was 11.02 m, whereas the maximum estimation error of the proposed solution was 3.75 m.

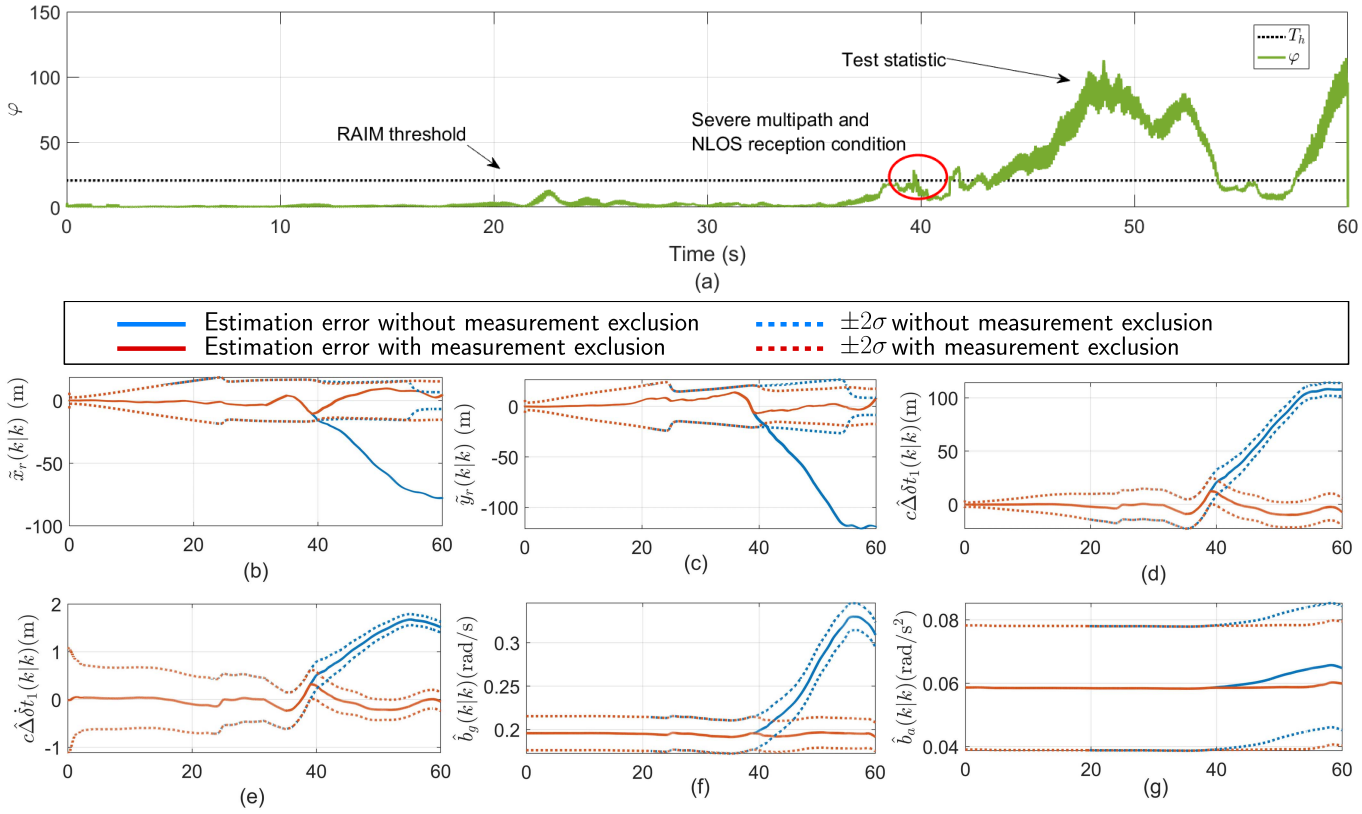

Fig. 14. Environment 1 experimental results: resulting fault detection test and exclusion; (a) the fault detection test which compares the test statistic φ against the detection threshold T_h, (b)–(c) the resulting position estimation errors and corresponding $\pm 2\sigma$ bounds with and without using the proposed fault exclusion, (d)–(e) the estimated receiver's clock error states, and (f)–(g) The resulting estimation and corresponding variances for IMU gyroscope and accelerometer biases.

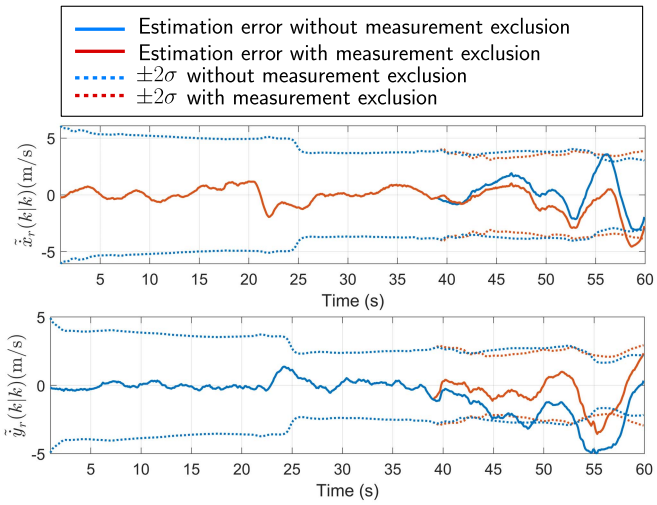

Fig. 15. Environment 1 experimental results: resulting velocity estimation error with and without using the proposed fault exclusion.

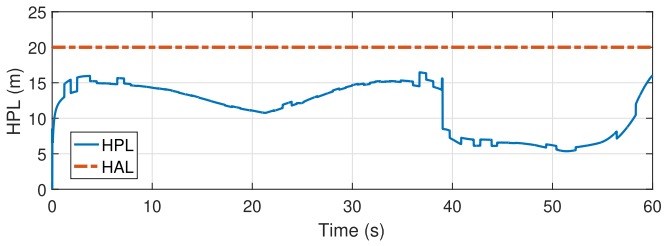

Fig. 16. Environment 1 experimental results: HPL and HAL over the course of the experiment.

Fig. 17 shows the vehicle's ground truth trajectory versus its estimated trajectories with and without measurement exclusion. It can be seen from Fig. 17 (a) that the proposed framework outperforms the navigation solution which does not include fault exclusion. Fig. 17 (b) compares the true range and the pseudorange drawn from the faulty tower (i.e., second tower) at the moment of fault occurrence. As expected, when a fault happens, a bias with a large magnitude is added to the pseudorange measurement. This bias may be particulary hazardous for fully autonomous ground vehicles. In contrast, the proposed framework did not exhibit such bias as the faulty measurement was excluded from the navigation solution. In order to identify the source of this bias, the channel impulse response is investigated, which is demonstrated in Fig. 17 (c). It can be seen that the receiver failed to detect the LOS peak as it has significantly less power than the non-LOS components (see the red circle in Fig. 17 (d)).

C. Environment 2 Experimental Results

In the second experiment, the performance of the proposed system in a more challenging scenario was assessed. This test

TABLE II
COMPARISON BETWEEN THE NAVIGATION SOLUTIONS WITH AND WITHOUT FAULT EXCLUSION

	Method 1	Method 2	Method 3 (Proposed)
Using fault exclusion	No	Yes	Yes
Using multipath model	No	No	Yes
RMSE	11.08 m	6.86 m	5.82 m
Standard deviation	11.02 m	5.14 m	3.75 m
Reduction in RMSE over Method 1	–	53.36%	65.97 %

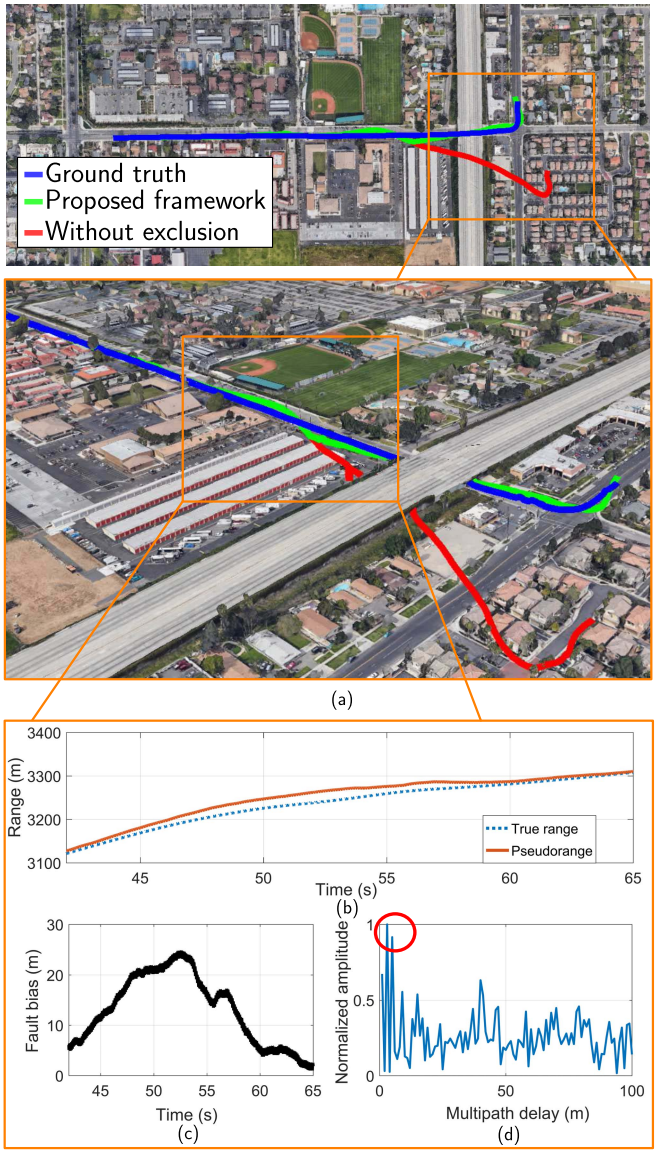

Fig. 17. Environment 1 experimental results: (a) A comparison between the vehicle's ground truth trajectory versus its estimated trajectories with and without measurement exclusion. As can be seen, the proposed framework outperforms the navigation solution without measurement exclusion. (b) The recorded true range versus pseudorange. (c) The fault bias added to the measurement. (d) Receiver CIR.

was performed in a deep urban environment in downtown Riverside, California, USA, where only 2 LTE transmitters where available. Only GPS signals were used in the GNSS-IMU system. The GPS signals were available at the start of the test; however, these signals were discarded over a portion of 40 m of the total trajectory to emulate a GPS unavailability condition. Fig. 18 shows the experimental environment, the location of the LTE towers, and the vehicle's ground truth trajectory (obtained with the GNSS-IMU system) versus that estimated with the proposed framework and that estimated with the GPS-IMU system. Similar to the first experiment, the fault detection and exclusion were performed throughout this experimental test. Fig. 19 (a) and Fig. 19 (b) show the resulting φ against the detection threshold T_h and the resulting protection level, respectively. It is worth noting that

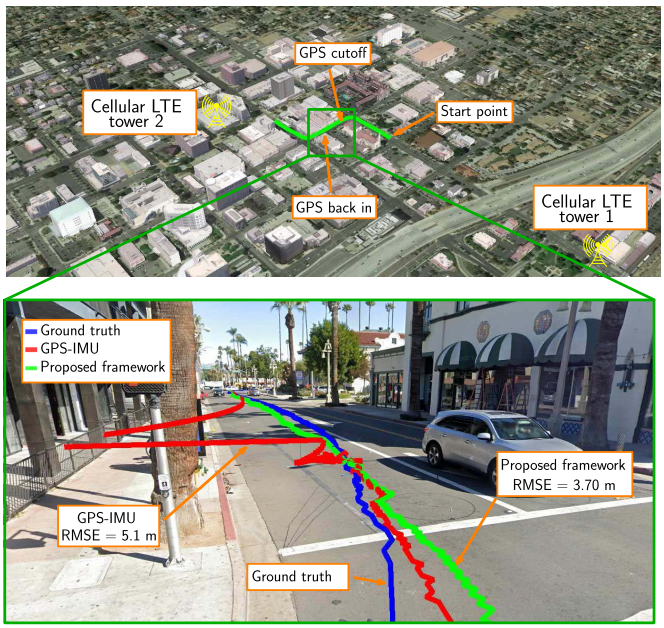

Fig. 18. Environment 2 experimental results: environment layout, LTE SOP tower locations, true vehicle trajectory, and the different navigation solutions, where the estimated vehicle position obtained from GPS-IMU and the proposed method are shown using red and green lines, respectively. In this experiment, the vehicle-mounted receiver traversed 345 m in an urban streets while listening to only 2 LTE SOPs simultaneously. Image: Google Earth.

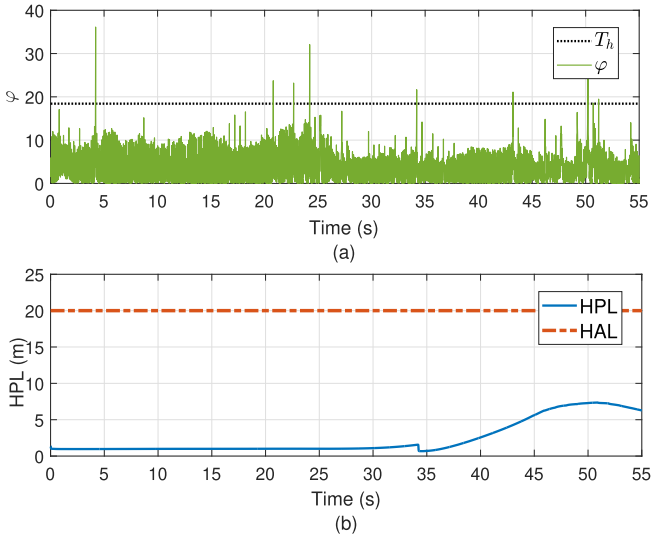

Fig. 19. Environment 2 experimental results: resulting fault detection test and exclusion; (a) the fault detection test which compares the test statistic φ against the detection threshold T_h, (b) The HPL and HAL over the course of the experiment.

in real-world scenarios, it is not practical to adaptively switch between faulty operation and fault-free operation based upon a single φ value outside the T_h, as this may cause numerous unnecessary switches based upon a single spike in φ value. Hence, instead of switching between faulty operation and fault-free operation based upon a single φ, a sliding window that includes the last 10 φ values was considered. The faulty operation is declared if and only if all φ elements inside a sliding window exceed the threshold. This can simply filter out the noisy spikes that superimpose φ, which are clearly visible in Fig. 19 (a) (compare to Fig. 14 (a), where φ exceeded T_h for long period of time). The implementation of sliding window of φ has been demonstrated in Fig. 3. In this experiment, the test φ was not declared fail, which implies that the LTE measurements are not faulty. The contribution of these two LTE measurements to the navigation solution can be seen in Fig. 18. As shown in Fig. 18, the GPS-IMU system achieved a RMSE of 5.1 m, while the RMSE obtained by the proposed framework was 3.7 over the same trajectory. Hence, using LTE measurements that have been validated by the RAIM framework presented in this paper, reduced the position RMSE by 27.45%.

VII. Conclusion and Discussions

This paper developed an autonomous integrity monitoring framework for ground vehicle navigation with cellular SOPs. To this end, an EKF-based RAIM framework was proposed which used IMU data and pseudoranges extracted from ambient cellular LTE towers. In contrast to previous work, the proposed framework did not use a stationary agent (i.e., base), to estimate the SOPs' clock error states; instead, it estimated the dynamic stochastic clock error states in a radio SLAM fashion. The proposed framework characterized two main sources of cellular pseudorange errors: (i) short multipath delays and (ii) unmodeled biases due to LOS signal blockage. The framework formulated a RAIM-based integrity monitoring to calculate the HPL and to exclude the faults occurrence due to LOS signal blockage and high signal attenuation. This paper assumed that only one measurement fault exists. For complicated wireless environments with multiple faults, more sophisticated methods such as advanced RAIM (ARAIM) must be employed. Experimental results over a total traversed trajectory of 825 m validated the efficacy of the proposed framework and also showed that the proposed measurement exclusion technique reduced the position RMSE by 66%.

Acknowledgment

The authors would like to thank K. Shamaei for her help with the data collection.

References

[1] M. Li and A. I. Mourikis, "High-precision, consistent EKF-based visual-inertial odometry," *Int. J. Robot. Res.*, vol. 32, no. 6, pp. 690–711, May 2013.

[2] L. Chang, X. Niu, T. Liu, J. Tang, and C. Qian, "GNSS/INS/LiDAR-SLAM integrated navigation system based on graph optimization," *Remote Sens.*, vol. 11, no. 9, p. 1009, Apr. 2019.

[3] H. Min, X. Wu, C. Cheng, and X. Zhao, "Kinematic and dynamic vehicle model-assisted global positioning method for autonomous vehicles with low-cost GPS/camera/in-vehicle sensors," *IEEE Sensors J.*, vol. 19, no. 24, pp. 1–24, Jan. 2019.

[4] H. Ko, B. Kim, and S.-H. Kong, "GNSS multipath-resistant cooperative navigation in urban vehicular networks," *IEEE Trans. Veh. Technol.*, vol. 64, no. 12, pp. 5450–5463, Dec. 2015.

[5] X. Chen and Y. Morton, "Iterative subspace alternating projection method for GNSS multipath DOA estimation," *IET Radar, Sonar Navigat.*, vol. 10, no. 7, pp. 1260–1269, Aug. 2016.

[6] J. Raquet and R. K. Martin, "Non-GNSS radio frequency navigation," in *Proc. IEEE Int. Conf. Acoust., Speech Signal Process.*, Mar. 2008, pp. 5308–5311.

[7] Z. M. Kassas, "Collaborative opportunistic navigation," *IEEE Aerosp. Electron. Syst. Mag.*, vol. 28, no. 6, pp. 38–41, Jun. 2013.

[8] Z. M. Kassas, "Analysis and synthesis of collaborative opportunistic navigation systems," Ph.D. dissertation, Dept. Elect. Comput. Eng., Univ. Texas Austin, Austin, TX, USA, 2014.

[9] S.-H. Fang, J.-C. Chen, H.-R. Huang, and T.-N. Lin, "Is FM a RF-based positioning solution in a metropolitan-scale environment? A probabilistic approach with radio measurements analysis," *IEEE Trans. Broadcast.*, vol. 55, no. 3, pp. 577–588, Sep. 2009.

[10] P. Thevenon *et al.*, "Positioning using mobile TV based on the DVB-SH standard," *Navigation*, vol. 58, no. 2, pp. 71–90, Jun. 2011.

[11] J. Khalife and Z. M. Kassas, "Navigation with cellular CDMA signals—Part II: Performance analysis and experimental results," *IEEE Trans. Signal Process.*, vol. 66, no. 8, pp. 2204–2218, Apr. 2018.

[12] Z. Kassas, J. Morales, and J. Khalife, "New-age satellite-based navigation—STAN: Simultaneous tracking and navigation with LEO satellite signals," *Inside GNSS Mag.*, vol. 14, no. 4, pp. 56–65, 2019.

[13] Z. M. Kassas, J. Khalife, K. Shamaei, and J. Morales, "I hear, therefore i know where i am: Compensating for GNSS limitations with cellular signals," *IEEE Signal Process. Mag.*, vol. 34, no. 5, pp. 111–124, Sep. 2017.

[14] K. Shamaei, J. Khalife, and Z. M. Kassas, "Exploiting LTE signals for navigation: Theory to implementation," *IEEE Trans. Wireless Commun.*, vol. 17, no. 4, pp. 2173–2189, Apr. 2018.

[15] M. Maaref and Z. M. Kassas, "Measurement characterization and autonomous outlier detection and exclusion for ground vehicle navigation with cellular signals," *IEEE Trans. Intell. Vehicles*, vol. 5, no. 4, pp. 670–683, Dec. 2020.

[16] C. Yang and T. Nguyen, "Tracking and relative positioning with mixed signals of opportunity," *Navigation*, vol. 62, no. 4, pp. 291–311, Dec. 2015.

[17] K. Shamaei and Z. Kassas, "LTE receiver design and multipath analysis for navigation in urban environments," *Navigat., J. Inst. Navigat.*, vol. 65, no. 4, pp. 655–675, Dec. 2018.

[18] J. Khalife and Z. M. Kassas, "Precise UAV navigation with cellular carrier phase measurements," in *Proc. IEEE/ION Position, Location Navigat. Symp. (PLANS)*, Apr. 2018, pp. 978–989.

[19] J. J. Khalife, S. Bhattacharya, and Z. M. Kassas, "Centimeter-accurate UAV navigation with cellular signals," in *Proc. 31st Int. Tech. Meeting Satell. Division Inst. Navigat. (ION GNSS+)*, Oct. 2018, pp. 2321–2331.

[20] K. Shamaei and Z. M. Kassas, "Sub-meter accurate UAV navigation and cycle slip detection with LTE carrier phase measurements," in *Proc. 32nd Int. Tech. Meeting Satell. Division Inst. Navigat. (ION GNSS+)*, Oct. 2019, pp. 2469–2479.

[21] R. Toledo-Moreo, D. Betaille, and F. Peyret, "Lane-level integrity provision for navigation and map matching with GNSS, dead reckoning, and enhanced maps," *IEEE Trans. Intell. Transp. Syst.*, vol. 11, no. 1, pp. 100–112, Mar. 2010.

[22] A. Ene, J. Blanch, and T. Walter, "Galileo-GPS RAIM for vertical guidance," in *Proc. Nat. Tech. Meeting Inst. Navigat.*, Jan. 2006, pp. 18–20.

[23] T. Walter, J. Blanch, M. J. Choi, T. Reid, and P. Enge, "Incorporating GLONASS into aviation RAIM receivers," in *Proc. Int. Tech. Meeting Inst. Navigat.*, Jan. 2013, pp. 239–249.

[24] P. F. Roysdon and J. A. Farrell, "GPS-INS outlier detection & elimination using a sliding window filter," in *Proc. Amer. Control Conf. (ACC)*, May 2017, pp. 1244–1249.

[25] A. V. Kanhere and G. X. Gao, "Integrity for GPS/LiDAR fusion utilizing a RAIM framework," in *Proc. 31st Int. Tech. Meeting Satell. Division Inst. Navigat. (ION GNSS+)*, Oct. 2018, pp. 3145–3155.

[26] Q. Sun and J. Zhang, "RAIM method for improvement on GNSS reliability and integrity," in *Proc. IEEE/AIAA 28th Digit. Avionics Syst. Conf.*, Oct. 2009, pp. 3–11.

[27] L. Zhang, J. Li, T. Cui, and S. Liu, "An adapted RAIM algorithm for urban canyon environment," in *Proc. Forum Cooperat. Positioning Service (CPGPS*, May 2017, pp. 116–121.

[28] D. Salos, "Integrity monitoring applied to the reception of GNSS signals in urban environments," Ph.D. dissertation, Nat. Polytech. Inst. Toulouse, Univ. Toulouse, Toulouse, France, 2012.

[29] S. Khanafseh, N. Roshan, S. Langel, F.-C. Chan, M. Joerger, and B. Pervan, "GPS spoofing detection using RAIM with INS coupling," in *Proc. IEEE/ION Position, Location Navigat. Symp. (PLANS)*, May 2014, pp. 1232–1239.
[30] M. Maaref, J. Khalife, and Z. M. Kassas, "Integrity monitoring of LTE signals of opportunity-based navigation for autonomous ground vehicles," in *Proc. 31st Int. Tech. Meeting Satell. Division Inst. Navigat. (ION GNSS+)*, Oct. 2018, pp. 2456–2466.
[31] J. J. Morales, P. F. Roysdon, and Z. M. Kassas, "Signals of opportunity aided inertial navigation," in *Proc. 29th Int. Tech. Meeting Satell. Division Inst. Navigat. (ION GNSS+)*, Nov. 2016, pp. 1492–1501.
[32] J. J. Morales and Z. M. Kassas, "Tightly-coupled inertial navigation system with signals of opportunity aiding," *IEEE Trans. Aerosp. Electron. Syst.*, Jan. 2021. [Online]. Available: https://ieeexplore.ieee.org/document/9335262
[33] R. Brown, "Receiver autonomous integrity monitoring," in *Global Positioning System: Theory and Applications*, vol. 2. Washington, DC, USA: American Institute of Aeronautics and Astronautics, 1996, ch. 5, pp. 143–165.
[34] J. Liu, M. Lu, X. Cui, and Z. Feng, "Theoretical analysis of RAIM in the occurrence of simultaneous two-satellite faults," *IET Radar, Sonar Navigat.*, vol. 1, no. 2, pp. 92–97, Apr. 2007.
[35] M. Joerger and B. Pervan, "Integrity risk of Kalman filter-based RAIM," in *Proc. ION GNSS Conf.*, Sep. 2011, pp. 3856–3867.
[36] D. Salós, A. Martineau, C. Macabiau, B. Bonhoure, and D. Kubrak, "Receiver autonomous integrity monitoring of GNSS signals for electronic toll collection," *IEEE Trans. Intell. Transp. Syst.*, vol. 15, no. 1, pp. 94–103, Feb. 2014.
[37] S. Bhattacharyya and D. Gebre-Egziabher, "Kalman filter–based RAIM for GNSS receivers," *IEEE Trans. Aerosp. Electron. Syst.*, vol. 51, no. 3, pp. 2444–2459, Jul. 2015.
[38] S. Bhamidipati and G. X. Gao, "SLAM-based integrity monitoring using GPS and fish-eye camera," in *Proc. 32nd Int. Tech. Meeting Satell. Division Inst. Navigat. (ION GNSS+)*, Oct. 2019, pp. 4116–4129.
[39] M. Joerger and B. Pervan, "Fault detection and exclusion using solution separation and chi-squared ARAIM," *IEEE Trans. Aerosp. Electron. Syst.*, vol. 52, no. 2, pp. 726–742, Apr. 2016.
[40] N. Zhu, J. Marais, D. Betaille, and M. Berbineau, "GNSS position integrity in urban environments: A review of literature," *IEEE Trans. Intell. Transp. Syst.*, vol. 19, no. 9, pp. 2762–2778, Sep. 2018.
[41] E. Kaplan and C. Hegarty, *Understanding GPS: Principles and Applications*, 2nd ed. Norwood, MA, USA: Artech House, 2005.
[42] K. Shamaei, J. Khalife, and Z. M. Kassas, "Comparative results for positioning with secondary synchronization signal versus cell specific reference signal in LTE systems," in *Proc. Int. Tech. Meeting Inst. Navigat.*, Mar. 2017, pp. 1256–1268.
[43] Z. Kassas, V. Ghadiok, and T. Humphreys, "Adaptive estimation of signals of opportunity," in *Proc. ION GNSS Conf.*, Sep. 2014, pp. 1679–1689.
[44] J. J. Morales and Z. M. Kassas, "Optimal collaborative mapping of terrestrial transmitters: Receiver placement and performance characterization," *IEEE Trans. Aerosp. Electron. Syst.*, vol. 54, no. 2, pp. 992–1007, Apr. 2018.
[45] Z. M. Kassas and T. E. Humphreys, "Observability analysis of collaborative opportunistic navigation with pseudorange measurements," *IEEE Trans. Intell. Transp. Syst.*, vol. 15, no. 1, pp. 260–273, Feb. 2014.
[46] J. Barnes *et al.*, "Characterization of frequency stability," *IEEE Trans. Instrum. Meas.*, vol. 20, no. 2, pp. 105–120, May 1971.
[47] Y. Bar-Shalom, X. Li, and T. Kirubarajan, *Estimation with Applications to Tracking and Navigation*. New York, NY, USA: Wiley, 2002.
[48] A. Thompson, J. Moran, and G. Swenson, *Interferometry and Synthesis in Radio Astronomy*, 2nd ed. Hoboken, NJ, USA: Wiley, 2001.
[49] J. A. del Peral-Rosado *et al.*, "Software-defined radio LTE positioning receiver towards future hybrid localization systems," in *Proc. 31st AIAA Int. Commun. Satell. Syst. Conf.*, Oct. 2013, pp. 14–17.
[50] C. Yang, T. Nguyen, and E. Blasch, "Mobile positioning via fusion of mixed signals of opportunity," *IEEE Aerosp. Electron. Syst. Mag.*, vol. 29, no. 4, pp. 34–46, Apr. 2014.
[51] J. Farrell and M. Barth, *The Global Positioning System and Inertial Navigation*. New York, NY, USA: McGraw-Hill, 1998.
[52] P. Groves, *Principles of GNSS, Inertial, and Multisensor Integrated Navigation Systems*, 2nd ed. Norwood, MA, USA: Artech House, 2013.
[53] M. Shelley, "Monocular visual inertial odometry," M.S. thesis, Dept. Inform., Tech. Univ. Munich, Munich, Germany, 2014.
[54] M. Maaref, J. Khalife, and Z. M. Kassas, "Lane-level localization and mapping in GNSS-challenged environments by fusing lidar data and cellular pseudoranges," *IEEE Trans. Intell. Vehicles*, vol. 4, no. 1, pp. 73–89, Mar. 2019.
[55] D. Salos, C. Macabiau, A. Martineau, B. Bonhoure, and D. Kubrak, "Analysis of GNSS integrity requirements for road user charging applications," in *Proc. Satell. Navigat. Technol. Eur. Workshop GNSS Signals Signal Process.*, Dec. 2010, pp. 1–8.
[56] B. Yang, K. B. Letaief, R. S. Cheng, and Z. Cao, "Timing recovery for OFDM transmission," *IEEE J. Sel. Areas Commun.*, vol. 18, no. 11, pp. 2278–2291, Nov. 2000.
[57] *Bbbike Extrats Service*. Accessed: 2021. [Online]. Available: https://extract.bbbike.org
[58] M. Maaref and Z. Kassas, "UAV integrity monitoring measure improvement using terrestrial signals of opportunity," in *Proc. ION Global Navigat. Satell. Syst. Conf.*, 2019, pp. 3045–3056.
[59] D. Simon, "Additional topics in Kalman filtering," *Optimal State Estimation: Kalman, H Infinity, and Nonlinear Approaches*. New York, NY, USA: Wiley, 2006, pp. 297–332.
[60] J. Blanch *et al.*, "Advanced RAIM user algorithm description: Integrity support message processing, fault detection, exclusion, and protection level calculation," in *Proc. ION GNSS Conf.*, Sep. 2012, pp. 2828–2849.
[61] G. Schroth, M. Rippl, A. Ene, J. Blanch, B. Belabbas, T. Walter, P. Enge, and M. Meurer, "Enhancements of the range consensus algorithm (ranco)," in *Proc. ION GNSS Conf.*, Sep. 2008, pp. 93–103.
[62] A. Grosch, O. Garcia Crespillo, I. Martini, and C. Gunther, "Snapshot residual and Kalman filter based fault detection and exclusion schemes for robust railway navigation," in *Proc. Eur. Navigat. Conf. (ENC)*, May 2017, pp. 36–47.
[63] (2018). *Septentrio AsteRx-i V*. [Online]. Available: https://www.septentrio.com/products
[64] Z. M. Kassas, M. Maaref, J. J. Morales, J. J. Khalife, and K. Shamei, "Robust vehicular localization and map matching in urban environments through IMU, GNSS, and cellular signals," *IEEE Intell. Transp. Syst. Mag.*, vol. 12, no. 3, pp. 36–52, Jun. 2020.
[65] M. Maaref and Z. Kassas, "Ground vehicle navigation in GNSS-challenged environments using signals of opportunity and a closed-loop map-matching approach," *IEEE Trans. Intell. Transp. Syst.*, vol. 21, no. 7, pp. 2723–2738, Jul. 2020.

Mahdi Maaref received the B.S. and M.S. degrees from the University of Tehran, in 2008 and 2011, respectively, and the Ph.D. degree in electrical engineering from Shahid Beheshti University, in 2016. He was a Visiting Research Collaborator with the University of Alberta, Edmonton, Canada, in 2016. He is currently a Postdoctoral Research Fellow with the University of California, Irvine, and a member of the Autonomous Systems Perception Intelligent and Navigation (ASPIN) Laboratory. His research interests include autonomous ground vehicles, opportunistic perception, and autonomous integrity monitoring.

Zaher (Zak) M. Kassas (Senior Member, IEEE) received the B.E. degree in electrical engineering from Lebanese American University, the M.S. degree in electrical and computer engineering from The Ohio State University, and the M.S.E. degree in aerospace engineering and the Ph.D. degree in electrical and computer engineering from The University of Texas at Austin. He is currently an Associate Professor with the University of California, Irvine, and the Director of the Autonomous Systems Perception, Intelligence, and Navigation (ASPIN) Laboratory. He is also the Director of the U.S. Department of Transportation Center: CARMEN (Center for Automated Vehicle Research with Multimodal AssurEd Navigation), focusing on navigation resiliency and security of highly automated transportation systems. In 2018, he received the National Science Foundation (NSF) Faculty Early Career Development Program (CAREER) award, and in 2019, he received the Office of Naval Research (ONR) Young Investigator Program (YIP) award. He was a recipient of 2018 IEEE Walter Fried Award, 2018 Institute of Navigation (ION) Samuel Burka Award, and 2019 ION Col. Thomas Thurlow Award. He is an Associate Editor of the IEEE TRANSACTIONS ON AEROSPACE AND ELECTRONIC SYSTEMS and the IEEE TRANSACTIONS ON INTELLIGENT TRANSPORTATION SYSTEMS. His research interests include cyber-physical systems, estimation theory, navigation systems, autonomous vehicles, and intelligent transportation systems.